Whole-rock and zircon evidence for evolution of the Late Jurassic high Sr/Y Zhoujiapuzi granite, Liaodong Peninsula, North China Craton

Renyu Zeng [a, b,c] *, **Mark B. Allen** [c], **Xiancheng Mao** [d], **Jianqing Lai** [d], **Jie Yan** [a, b], **Jianjun Wan**[a, b]

[a] State Key Laboratory of Nuclear Resources and Environment, East China University of Technology, Nanchang, 330013, Jiangxi, China

[b] School of Earth Sciences, East China University of Technology, Nanchang, 330013, China

[c] Department of Earth Sciences, Durham University, Durham DH1 3LE, UK

[d] School of Geosciences and Info-Physics, Central South University, Changsha 410083, China

Correspondence: Renyu Zeng (zengrenyu@126.com)

Abstract: Middle-Late Jurassic high Sr/Y granitic intrusions are extensively exposed in the Liaodong Peninsula, in the eastern part of the North China Craton (NCC). However, the genesis of the high Sr/Y signature in these intrusions has not been studied in detail. In this study, we report results of zircon U-Pb dating, Hf isotopic analysis and zircon and whole-rock geochemical data for the Late Jurassic Zhoujiapuzi granite in the middle part of the Liaodong Peninsula. The Zhoujiapuzi granite is high-K (calc-alkaline) and peraluminous in nature, with high SiO_2 (68.1–73.0 wt %) and Al_2O_3

23 (14.5–16.8 wt %), low in TFe_2O_3 (1.10–2.49 wt %) and MgO (0.10–0.44 wt %), and

24 with high Sr/Y (19.9–102.0) and La_N/Yb_N (14.59–80.40), characteristic of high Sr/Y I-

25 type granite. The geochemical signatures, in combination with the presence of a large

26 number of Paleoproterozoic inherited zircons, indicate that the Zhoujiapuzi granite was

27 most likely derived from partial melting of the basement in the region, and specifically

28 the Liaoji granites. The high Sr/Y signature is inherited from these source rocks. LA-

29 ICP-MS zircon U-Pb dating of the autocryst zircons from two samples (from different

30 localities) yielded consistent weighted average ages of 160.7±1.1 Ma (MSWD=1.3) and

31 159.6±1.1 Ma (MSWD=1.2), with εHf(t) values in the range of -26.6– -22.8.

32 Morphological and chemical studies on autocrystic zircon grains show that there are

33 two stages of zircon growth, interpreted as magmatic evolution in two distinct stages.

34 The light-CL core reflects a crystallization environment of low oxygen fugacity and

35 high T_{Zr-Ti}; the dark-CL rim formed with high oxygen fugacity and lower T_{Zr-Ti}. Based

36 on the geochemical features and regional geological data, we propose that the Liaodong

37 Peninsula in the Late Jurassic was part of a mature continental arc, with extensive

38 melting of thick crust above the Paleo-Pacific subduction zone.

39 **Keywords:** Liaodong Peninsula; Late Jurassic; Zircon U-Pb-Hf isotopes; Two stages

40 of crystal growth; High Sr/Y granite

41 **1. Introduction**

42   The Liaodong Peninsula is located in the northeast of the North China Craton

43 (NCC). The northeast NCC was influenced by three main tectonic regimes in the

44 Mesozoic, related to the subduction of the Paleo-Asian, Paleo-Pacific and Mongol-

2

Okhotsk oceans (Tang et al., 2018). The superposition of these different regimes resulted in changing tectonic and magmatic patterns over time. Middle-Late Jurassic granitic rocks are extensively exposed in the northern parts of the Liaodong Peninsula, such as the Yutun mylonitic granite, Xiaoheishan granodiorite, Heigou monzogranite (Wu et al., 2005), Wulong two-mica monzogranite (Yang et al., 2018), and Huangdi biotite monzogranite (Xue et al., 2020). Most of these rocks are characterized by high Sr /Y, and plot within the adakite field on Sr/Y-Y and La_N/Yb_N-Yb_N diagrams (Wu et al., 2005a; Yang et al., 2015a, 2018).

The geodynamic settings and petrogenesis of adakite and geochemically similar high Sr/Y igneous rocks have been widely discussed. The high Sr/Y rocks were originally proposed to be formed by melting of young (<25 Ma) and hot subducted oceanic slab in an arc setting (Defant and Drummond, 1990). However, later studies have shown that the high Sr/Y rocks can form in both arc and non-arc settings by other processes, such as continental interior settings (Wang et al., 2007), cold subduction zones (Nakamura and Iwamori, 2013), collision or post-collision processes (Schwartz et al., 2011). In addition, numerous studies have suggested that the lower continental crust can also be the source of the high Sr/Y rocks (Gao et al., 2004; Ou et al., 2017). However, it is debated whether crustal thickening is necessary for their formation (e.g. Moyen, 2009; Kamei et al., 2009; Zhan et al., 2020). In recent years, some studies have proposed that the high Sr/Y ratio in granitic rocks can be inherited from a high Sr/Y crust source, regardless of pressure (Kamei et al., 2009; Ma et al., 2015; Zhan et al., 2020).

The Middle-Late Jurassic granitic rocks in the Liaodong Peninsula are commonly proposed to be the products of partial melting of thickened mafic crust with garnet in the residue (Wu et al., 2005a; Yang et al., 2015a, 2018; Tang et al., 2018). However, the

70   source composition has not been fully considered in the petrogenesis of the high Sr/Y

71   rocks in the Liaodong Peninsula. Hence, the petrogenesis of the Middle-Late Jurassic

72   high Sr/Y rocks needs to be re-evaluated, based on more detailed work and a

73   consideration of possible sources. This petrogenesis is of significance for understanding

74   the Jurassic tectonics of the Liaodong Peninsula, and the NCC in general.

75   In this paper, we examined the high Sr/Y Zhoujiapuzi granite from the Xiuyan area,

76   in the middle of the Liaodong Peninsula. Zircons are analysed for U-Pb-Hf isotopes

77   and trace element geochemistry, and by Raman spectroscopy. These results are

78   integrated with whole-rock geochemistry. We focus on the zircons, because of their

79   potential to reveal the origins of the pluton (Belousova et al., 2002; Wang et al., 2007;

80   Breiter et al., 2014; Zhao et al., 2014), and so provide a case study for the evolution of

81   plutonic magma systems in general. Based on observations of the CL images and

82   chemical analysis, two zircon growth stages can be distinguished. We first determine

83   the crystallization environments of the two zircon growth stages, and then decipher the

84   petrogenesis, source characteristics and origin of the high Sr/Y signature of the pluton

85   as a whole. Integrated with previous studies, our study provides insights into the

86   tectonic evolution of the Liaodong Peninsula in the Late Jurassic.

87   **2. Geological setting**

88   The Zhoujiapuzi granite is located in the middle of the Liaodong Peninsula, at the

89   northeastern margin of the NCC (Fig. 1). The Paleoproterozoic Liaohe Group and Liaoji

90   granite are the basement in the study area. The Liaohe Group includes the Lieryu,

91   Gaojiayu, Dashiqiao and Gaixian formations. Although stratigraphic terms are used,

92   these rocks are metamorphic, and the group consists of leptynite, leptite, granulite,

93 amphibolite, marble and phyllite. The protoliths of the Liaohe Group include marine

94 volcanics, clastics, carbonates and claystones. The formation age of the

95 metasedimentary rocks in the Liaohe Group is 2.0–1.9 Ga (Wan et al., 2006; Li et al.,

96 2015). It is in unconformable contact with the overlying strata of the Mesoproterozoic

97 Cuocaogou Formation and Xiaoling Formation.

98 The study area experienced strong magmatic activity in the Paleoproterozoic,

99 which can be divided into two stages of 2.2–2.1 Ga and ~ 1.85 Ga. The 2.18–2.14 Ga

100 Liaoji granites (also called gneissic granites), which lie within an area measuring 300

101 km × 70 km, are dominated by A- and I-type granites (Li and Zhao, 2007; Yang et al.,

102 2016; Wang et al., 2020a). Metamorphosed volcanic rocks (leptynite, leptite and

103 granulite) in the Liaohe Group also formed at 2.2–2.1 Ga (Li et al., 2015). The ~1.85

104 Ga granites mainly consist of I- and S-type porphyry granites and alkaline syenites

105 (Yang et al., 2007; Yang et al., 2015b). In addition, there were small amounts of mafic

106 magmatic activity at ~2.17 Ga, ~2.1 Ga and ~1.8 Ga (Meng et al., 2014; Yuan et al.,

107 2015). There are a variety of viewpoints on the Paleoproterozoic tectono-magmatic

108 evolution in the Liaodong Peninsula, such as an intracontinental rift opening-closing

109 model (Li et al., 2005) and an arc-continent collision model (Faure et al., 2004).

110 In the Mesozoic, the region of the Liaodong Peninsula was influenced by the

111 circum-Pacific tectonic regime, the Mongol-Okhotsk tectonic regime and the Paleo-

112 Asian Ocean tectonic regime. The joint influence of multiple tectonic regimes resulted

113 in intensive magmatism during the Mesozoic (Fig. 1b). These Mesozoic magmatic

114 rocks can be divided into three stages, namely: Triassic (233–212 Ma), Jurassic (180–

156 Ma) and Early Cretaceous (131–117 Ma) (Wu et al., 2005b).

The Triassic magmatic rocks are less exposed, mainly alkaline rocks, diabase, diorites and granites (Wu et al., 2005b). Among them, the granites mainly have A-type affinity, and may have formed in an extensional setting (Tang et al., 2018; Wang et al., 2019). Magmatism has been related to either the subduction of the Paleo-Pacific slab, closure of the Paleo-Asian Ocean, or the collision between the NCC and the Yangtze Craton (Tang et al., 2018; Wang et al., 2019). The majority of the Jurassic magmatic rocks are monzogranite and granodiorite, which are generally calc-alkaline I-type granites, and show characteristics of adakite-like rocks. Some of them, exposed near later extensional structures, have undergone regional ductile deformation. These Jurassic magmatic rocks are generally considered to relate to the subduction of the Paleo-Pacific slab (Wu et al., 2005a; Zhai et al., 2004). In the Early Cretaceous, basic-acidic-alkaline rocks were widely developed. Among them, the granites have mainly A- and I-type affinities. These rocks are generally considered to have formed in an intense extensional environment, which is connected with either the rollback or low-angle subduction of the Paleo-Pacific slab (Wu et al., 2005c; Zheng et al., 2018).

3. Samples and petrography

The Zhoujiapuzi granite is located to the east of Xiuyan City, in the middle of the Liaodong Peninsula (Fig. 1b). It intruded into the Lieryu Formation of the Liaohe Group. Eight samples of the Zhoujiapuzi granite were collected at locations shown in Fig. 1c.

The Zhoujiapuzi granite is generally grey in colour and with fine-grained texture

136 (Fig. 2a). The mineral assemblage contains K-feldspar (~50 %), quartz (~25 %),

137 plagioclase (~20 %) and biotite (~5 %) as well as accessory minerals such as zircon,

138 ilmenite, magnetite and apatite. K-feldspar grains are euhedral or subhedral, and always

139 exhibit cross-hatched twinning (Fig. 2b). Quartz grains are usually xenomorphic, and

140 have indented boundaries and wavy extinction (Fig. 2b-d). Plagioclase always exhibits

141 polysynthetic twinning and have sericitization in places (Fig. 2c). Biotite mainly fills

142 in the interstices between the other minerals (Fig. 2c, d).

143 **4. Analytical methods**

144 The cathodoluminescence (CL) images of zircon were obtained by the Chengpu

145 geological Testing Co. Ltd, Langfang, China using the TIMA analysis. The LA-ICP-

146 MS zircon U-Pb analyses were performedusing an Agilent Technologies 7700x ICP-

147 MS with a Teledyne Cetac Technologies Analyte Excite laser-ablation system at

148 Nanjing FocuMS Contract Testing Co. Ltd. The analyses were carried out with a 35 μm

149 spot size at 8 Hz repetition rate for 40 seconds. The ICP-MS detector has dual modes:

150 pulse for lower signal, and analog for higher signal. Pulse-analog cross calibration was

151 performed before the measurement of U-Pb isotopes, delivering a wider linear dynamic

152 range – up to 10 orders of magnitude. For a signal of ^{238}U higher than 1.2–1.4 Mio cps,

153 equivalent zircon contains U concentrations higher than 600 ppm, and are measured in

154 analog mode. 91500 was used as external standard. GJ-1 (600Ma, Jackson et al., 2004)

155 and Plešovice (337Ma, Sláma et al., 2008) were treated as quality control for

156 geochronology. During our analyses, the weighted mean age of GJ-1 and Plešovice

157 were 606.0 ± 4.8 Ma (n=16, MSWD = 0.50) and 340.9 ± 4.0 Ma (n=7, MSWD = 1.0),

158 respectively. Trace elements abundance of zircon were externally calibrated against

NIST SRM 610 with Si as the internal standard. The raw ICP-MS data were processed using ICPMSDataCal software (Liu et al., 2010). No common-Pb correction was applied to the data. Data reduction was completed using the Isoplot4.15 (Ludwig, 2003). The instrument description and analytical procedure are described in detail by Zeng et al. (2018).

The in-situ Lu-Hf isotopic analyses of zircon were performed by LA-MC-ICP-MS using a Teledyne Cetac laser-ablation system and a Nu Plasma II MC-ICP-MS at Nanjing FocuMS Contract Testing Co. Ltd. The 193 nm ArF excimer laser was focused on zircon surface with fluence of $6.0 J/cm^2$. The ablation protocol employed a spot diameter of 50 um at 8 Hz repetition rate for 40 seconds. Three standard zircons, GJ-1, 91500, and Penglai, were analysed for quality control at every ten unknown samples. In the experiment, standard zircon GJ-1, 91500, and Penglai were analyzed, and the $^{176}Hf/^{177}Hf$ ratios were 0.282002–0.282013, 0.282305–0.282315 and 0.282901–0.282914 respectively, in accordance with their recommended values (GJ-1: 0.282012, Yuan et al., 2008; 91500: 0.282307 ± 0.000031, Wu et al., 2006; Penglai: 0.282906 ± 0.000010, Li et al., 2010). For the calculation of εHf(t) values, we have adopted the ^{176}Lu decay constant of 1.867×10^{-11} (Söderlund et al., 2004), the present-day chondritic values of $^{176}Lu/^{177}Hf = 0.0332$ and $^{176}Hf/^{177}Hf = 0.282772$ (Blichert-Toft and Albarède 1997). To calculate one-stage model ages (T_{DM1}) relative to a depleted-mantle source, we have adopted the present-day depleted-mantle values of $^{176}Lu/^{177}Hf = 0.0384$ and $^{176}Hf/^{177}Hf = 0.28325$ (Vervoort and Blichert-Toft 1999). To calculate two-stage modal ages (TDM2), 'felsic crust' model ages are calculated using average continental crust $^{176}Lu/^{177}Hf = 0.015$ (Griffin et al., 2004)

182   Zircon Raman analyses were carried out using an RM2000 laser Raman

183   spectrometer at the State Key Laboratory of Nuclear Resources and Environment, East

184   China University of Technology. The selected incident wavelengths were 532 and 785

185   nm in order to clearly identify the luminescence bands due to low concentration

186   impurities. The beam power was 20 mW. The Leica 50× objective was employed.

187   Six fresh rock samples were selected for geochemical analysis. The elemental

188   analyses were conducted at Analytical Chemistry & Testing Services (ALS) Chemex

189   (Guangzhou) Ltd. Major oxides were analyzed using wave-dispersive X-ray

190   fluorescence (XRF) (ME-XRF26). Analytical precision was better than $\pm$ 0.01%.

191   Trace element abundances were measured by the lithium borate dissolution method and

192   ICP-MS (ME-MS81). The analytical uncertainties of the rare earth element (REE) and

193   high field strength element (HFSE) are <5%. Analytical uncertainties are in the range

194   of 5%–10% for the other elements. Detailed analytical procedures refer to Zhang et al.

195   (2019) and Nash et al. (2020).

196   **5. Analytical results**

197   The data for major and trace elements, Raman microprobe data, zircon trace

198   elements, zircon U-Pb ages, and zircon Hf isotopes are shown in Tables S1, S2, S3, S4

199   and S5, respectively.

200   **5.1. Whole-rock major and trace element compositions**

201   SiO_2 contents range from 68.11 wt.% to 73.02 wt.% (average 71.71 wt.%).

202   Contents of Na_2O and K_2O are 3.81－4.65 wt.% and 4.32－4.71 wt.%, respectively,

203 with Na_2O/K_2O ratio of 0.82–1.08 and total alkalis ($Na_2O + K_2O$) of 8.38–8.97. All

204 samples plot in the field of granite in the TAS classification except one (Fig. 3a). These

205 samples have Al_2O_3 contents of 14.49–16.83 wt.% (average 15.09 wt.%), CaO

206 contents of 1.04–1.98 wt.% (average 1.38 wt.%) and A/CNK values of 1.05–1.10

207 (average 1.07). In the A/NK–A/CNK diagram (Fig. 3b), all samples plot in the

208 peraluminous field (Fig. 3b). The granite samples have low TFe_2O_3 (TFe_2O_3 = all Fe

209 calculated as Fe_2O_3) contents and MgO contents ranging from 1.10–2.49 wt % and

210 0.10–0.44 wt %, respectively, with Mg# (Mg#=100*molar Mg/(Mg+Fe)) values of 15–

211 26.

212   The samples of the Zhoujiapuzi granite exhibit variable REEs, with total REEs

213 ranging from 59 to 302 ppm. The La_N/Yb_N values of the Zhoujiapuzi granite range from

214 14.59 to 80.40 (average 38.27), showing right-declined REE patterns (Fig. 4a). The

215 samples have Eu/Eu* of 0.62–1.94 and Ce/Ce* of 0.94–1.16. In the primitive mantle-

216 normalized trace element diagram (Fig. 4b), the samples show negative anomalies of

217 HFSEs (e.g., Nb, Ta, Ti and P) and positive anomalies of La and LILEs (e.g., K, Rb,

218 Ba, U, La, Ce). The Zhoujiapuzi granite is characterized by high contents of Sr (309–

219 551 ppm) and low contents of Y (5.01–15.5 ppm) and Yb (0.43–1.40 ppm), with high

220 Sr/Y ratios of 19.94–102.04 (average 65.50).

221 **5.2 Zircon CL images, Raman spectra and REE elements**

222   CL images of zircons from the Zhoujiapuzi granite are shown in Fig. 5. Zircons

223 commonly have crystal sizes between 150 and 250 μm, and have length/width ratios of

224 2:1–4:1, with euhedral, stubby to elongate prisms. According to the CL images, most

225 zircons show an internal division into 2 distinct domains: light-CL core and dark-CL

226 rim. The light-CL core is characterized by bright CL intensity and widely-spaced

227 oscillatory zoning patterns. The dark-CL rim is overgrown continuously by the light-

228 CL core and is characterized by extremely low CL emission and narrowly-spaced

229 oscillatory zoning patterns. In addition, some zircons have inherited cores, which have

230 corroded and rounded shapes in contact with the light-CL core, such as 1# and 37# in

231 XY-001 and 6# and 41# in XY-008 (Fig. 5). These inherited zircons have oscillatory

232 zoning in CL images.

233 Six light-CL core spots and six dark-CL rim spots were analyzed for Raman

234 spectra. The light-CL cores have antisymmetric stretching vibration (B_{1g}) of the SiO_4

235 tetrahedra (v_3 (SiO_4)) Raman band of 1005–1007 cm^{-1} and half-width of the v_3 (SiO_4)

236 Raman band (b) values of 6.0–8.1 cm^{-1}, while the dark-CL rims have v_3 (SiO_4) Raman

237 band of 1004–1007 cm^{-1} and b values of 5.4–9.0 cm^{-1}.

238 Twenty light-CL core spots, eighteen dark-CL rim spots and six inherited zircon

239 spots were analyzed for trace and rare earth elements. The light-CL core spots have

240 lower U content (28–677 ppm) than the dark-CL rim spots (U=641–3842 ppm). In the

241 chondrite-normalized REE element diagram (Fig. 6a, b), both the light-CL core and

242 dark-CL rim are characterized by HREE enrichment relative to LREE with positive Ce

243 anomalies and negative Eu anomalies. The light-CL core spots have ΣREE of 49–1115

244 ppm (average 390 ppm), ΣLREE of 3–72 ppm (average 14 ppm) and ΣHREE of 46–

245 1100 ppm (average 377 ppm), whereas the dark-CL rim spots have ΣREE of 327–1632

246 ppm (average 895 ppm), ΣLREE of 2–14 ppm (average 6 ppm) and ΣHREE of 325–

247 1627 ppm (average 889 ppm). Hence, the REE content of the light-CL core is

248 significantly lower than that of the dark-CL rim, and the difference between the two is

249 mainly in HREE content. The light-CL core spots have Eu/Eu* of 0.07–0.60 (average

250 0.28) and Ce/Ce* of 1.89–24.27 (average 10.03). Because the contents of La and Pr are

251 typically present very low, Ce* in this study is obtained by the formulation $(Nd_N)^2/Sm_N$

252 (Loader et al., 2017). The dark-CL rim spots have Eu/Eu* of 0.08–0.24 (average 0.13)

253 and Ce/Ce* of 6.57–200.31 (average 79.23). These results indicate that the light-CL

254 core have a weaker negative Eu anomaly and a weaker positive Ce anomaly than those

255 of the dark-CL rim. The inherited zircon spots have ΣREE of 602–1517 ppm, and show

256 depletion of LREE, enrichment of HREE, a positive Ce anomaly (Ce/Ce* of 1.52–

257 216.08) and a negative Eu anomaly (Eu/Eu* of 0.07–0.13) (Fig. 6c).

5.3 Zircon U–Pb and Hf isotope composition

259 Seventy-seven spots were analysed for U-Pb isotope composition from samples

260 XY-001 and XY-008. In the U-Pb Concordia diagram (Fig. 7a, c), both the light-CL

261 core and dark-CL rim spots overlap within uncertainty on the Concordia curve. There

262 is a large degree of overlap between the 29 spots of dark-CL rim and 32 spots of light-

263 CL core in terms of $^{206}Pb/^{238}U$ age although the average value for $^{206}Pb/^{238}U$ age is

264 higher in the 32 spots of light-CL core (Fig. 7e). On a single zircon, the $^{206}Pb/^{238}U$ age

265 of the light-CL core is older than that of the dark-CL rim (Fig. 5), but the two values

266 are within the error range of the in-situ LA-ICP-MS analyses (individual spot of $\pm$3–5%

267 relative precision, Schmitz and Kuiper, 2013). In sample XY-001, 33 spots define a

268 weighted mean $^{206}Pb/^{238}U$ age of 160.7$\pm$1.1 Ma (2σ, MSWD=1.3; Fig. 7b). In sample

269 XY-008, 28 spots define a weighted mean $^{206}Pb/^{238}U$ age of 159.6$\pm$1.1 Ma (2σ,

270 MSWD=1.2; Fig. 7d). The other 10 spots with distinctly older ages ($^{207}Pb/^{206}Pb$ ages

271 ranging from 2500 to 2173 Ma) were obtained on inherited cores. Their ages are

272 discordant, suggesting that these inherited cores were variably influenced by lead loss.

273 Among these, 9 spots define a discordia line with an upper intercept age of 2163 $\pm$ 13

274 Ma (MSWD=0.45) (Fig. 7f).

275   Twenty-four zircons were analyzed for Lu-Hf isotope composition. The variation

276   in Hf isotopic data is limited, between 9 spots from light-CL core and 9 spots from dark-

277   CL rim. 18 spots exhibit a range of $^{176}Hf/^{177}Hf$ ratios from 0.281921 to 0.282030, which

278   converts to εHf(t) values between -26.6 to -22.8 (Fig. 8), and two-stage Hf model (T_{DM2})

279   ages of 2650 to 2889 Ma by using the U-Pb age for each zircon. Six analytical spots,

280   which define the Concordia upper intercept age of 2163 Ma, show $^{176}Hf/^{177}Hf$ radios

281   and εHf(t) values of 0.281443 to 0.281496 and -0.7 to 1.5, respectively, with T_{DM2} age

282   of 2648 Ma to 2791 Ma by using the upper intercept age.

283   **6. Discussion**

284   **6.1 Significance of the two stages of zircon**

285   Generally, zircon with high U content can easily break down into the metamict

286   state because of the radiation damage to the lattice caused by α-particles originating

287   from the decay of uranium (Mezger and Krogstad, 1997). The physical and structural

288   changes often lead to the loss of Pb and addition of trace elements such as LREE. In

289   this study, the dark-CL rim spots have high U content, which is significantly higher than

290   the median value of zircon U content in granitic magma (350 ppm, Wang et al., 2011).

291   Hence, the metamictization degree of the zircons must be taken into consideration. Data

292   from dark-CL rim spots plot on the Concordia curve, indicating no obvious Pb loss. The

293   internal structure of dark-CL rim is relatively intact, with obvious oscillatory zoning,

294   and few cracks, implying that the physical and structural of the dark-CL rim remained

295   unchanged. Nasdala et al. (1998) suggested that the metamictization of zircon can be

296   well characterized by Raman spectroscopy. The half-width of the $v_3(SiO_4)$ Raman band

297   (*b*) of 10 cm^{-1} and 20 cm^{-1} are proposed to approximately distinguish well-crystallized,

298   intermediate and metamict zircons (Nasdala et al., 1998). The dark-CL rim have *b*

299   values of 5.4–9.2, characterizing them as well-crystallized. Therefore, the above

300   features indicate that the dark-CL rim are not metamict. Consequently, it can be

301   concluded that the U-Pb isotope and trace element systematics of the dark-CL rim have

302   not been changed by metamictization.

303   Both the light-CL core and dark-CL rim have oscillatory zoning patterns, and their

304   chondrite-normalized REE patterns are characterized by steeply positive slopes from

305   the LREE to HREE with strong negative Eu anomalies and pronounced positive Ce

306   anomalies. The above characteristics are consistent with those of igneous zircon

307   (Hoskin and Schaltegger, 2003). Although hydrothermal zircon can also have

308   oscillatory zoning patterns similar to magmatic zircons, there are obvious differences

309   in trace elements between the magmatic and hydrothermal zircon (Hoskin et al., 2005).

310   In the discrimination diagram (Fig. 9), both the spots of light-CL core and dark-CL rim

311   fall in or near the magmatic field, which is obviously different from hydrothermal

312   zircon. Hence, the above characteristics indicate that both the light-CL core and dark-

313   CL rim have a magmatic origin.

314   The light-CL core was overgrown continuously by the dark-CL rim. In addition,

315   the contact between the light-CL core and dark-CL rim is euhedral. Such core-mantle

316   overgrowth relationships indicate that the light-CL core domains are not inherited

317   zircons. The similar Hf isotopic data of the light-CL core and dark-CL rim is also

318   consistent with this interpretation. For the age population, the samples of XY-001 and

14

319 XY-008 have MSWD of 1.3 and 1.2, respectively, which are both within the expected

320 range for 95 % confidence interval (Mahon, 1996). Although the $^{206}Pb/^{238}U$ age of dark-

321 CL rim is generally younger than that of light-CL core, the ages of these two distinct

322 domains have the characteristics of continuous variation, and do not show two or more

323 distinct age populations (Fig. 7b, d). These phenomena do not support the presence of

324 antecrystic zircons (Siégel et al., 2018). Hence, both the light-CL core and dark-CL rim

325 are most likely autocrystic zircon formed in one distinct pulse of magma. The weighted

326 mean U-Pb ages of 160.7±1.1 Ma and 159.6±1.1 Ma can be interpreted as the

327 emplacement age of the Zhoujiapuzi granite. The obvious difference in internal

328 structure and trace element composition between the light-CL core and dark-CL rim

329 could be due to significant changes in their crystallization environments (Wang et al.,

330 2007).

331   The Zr/Hf ratio in zircon has a negative correlation with the degree of fractionation

332 in the parent melt (Claiborne et al., 2006). In this study, the Zr/Hf ratios of the dark-CL

333 rim (21–40) are obviously lower than those of the light-CL core (39–56) (Fig. 10a). In

334 addition, incompatible elements such as U and REE will become enriched in the highly

335 evolved magma (Zhao et al., 2014). In this study, the contents of U and REE of dark-

336 CL rim are significantly higher than those of light-CL core (Fig. 10a). Overall, the

337 above features reflect that the dark-CL rim crystallized from a later and more evolved

338 magma.

339   Watson and Harrison (2005) found that the Ti content of zircon has a strong

340 dependence on temperature (T), and obtained a Ti-in-zircon thermometer (T_{Zr-Ti}). Since

341 then, Ferry and Watson (2007) suggested that the solubility of Ti in zircon depends not

342 only on T and activity of TiO_2 ($aTiO_2$) but also on the activity of SiO_2 ($aSiO_2$), and

343 revised the T_{Zr-Ti}. We use the T_{Zr-Ti} from Ferry and Watson (2007) and the recommended

344 values ($aSiO_2=1$, $aTiO_2 = 0.5$) for the activity of SiO_2 and TiO_2 (Schiller and Finger,

345 2019), due to the presence of ilmenite and quartz in the Zhoujiapuzi granite. The T_{Zr-Ti}

346 from the light-CL core and dark-CL rim are 684–830 °C (average 761 °C) and 509–

347 712°C (average 635 °C), respectively, i.e. the light-CL core formed at higher

348 temperatures than the dark-CL rim. The T_{Zr-Ti} value shows a significant positive

349 correlation with Zr/Hf (a tracer of fractional crystallisation), and shows continual

350 fractionation and cooling (Fig. 10b). As the light-CL core and dark-CL rim formed in

351 different magmatic evolution stages, it is problematic to use the same $aSiO_2$ and $aTiO_2$

352 values to calculate both T_{Zr-Ti} values for both. For ilmenite bearing granites, Schiller

353 and Finger (2019) suggested that the variation of $aTiO_2$ values corresponding to

354 different zircon crystallization stages is small. In addition, Schiller and Finger (2019)

355 showed that the $aSiO_2$ value of the ilmenite-bearing granites at the onset of magmatic

356 zircon crystallization was more than 0.75. Even if the $aSiO_2$ value of the light-CL core

357 is changed from 1.0 to 0.75, the temperature will only drop by about ~27 ℃, which is

358 significantly lower than the 126 °C difference between the average T_{Zr-Ti} value of the

359 light-CL core and dark-CL rim. Therefore, it is certain that the light-CL core formed at

360 higher temperatures than the dark-CL rim, although we cannot calculate the specific

361 temperature difference.

362 　　Cerium exists in magmas as both Ce^{3+} and Ce^{4+}. Because the 0.84-Å radius of the

363 Zr^{4+} ion is more closely matched by the Ce^{4+} (0.97-Å radius) than the Ce^{3+} (1.143-Å

364 radius) (all ionic radii are from Shannon, 1976), Ce^{4+} is more compatible in the zircon

365 structure than the Ce^{3+}. Hence, the magnitude of Ce anomaly is a useful tool for

366 evaluating the oxygen fugacity condition of crystallization environment (e.g. Ballard et

367 al., 2002; Trail et al., 2012). Loader et al. (2017) suggested that the Ce/Ce* ratio is

368 likely to be the most robust measure of magma redox conditions, although it is only a

369 semi-quantitative measure. In this study, the Ce/Ce* ratio of the light-CL core and dark-

370 CL rim are 6.30–153.36 (average 32.51) and 21.81–5773.06 (average 787.39),

371 respectively. This result suggests that the dark-CL rim formed in a higher oxygen

372 fugacity environment than the light-CL core. As shown in the Ce/Ce*-Zr/Hf diagram

373 (Fig. 10c), Ce/Ce* has a significant negative correlation with Zr/Hf, showing that the

374 oxygen fugacity condition is increasing with the evolution of magma.

375 The absence of enclaves and disequilibrium textures in the Zhoujiapuzi granite

376 and uniform εHf(t) values of the light-CL core and dark-CL rim do not support magma

377 mixing and wall-rock assimilation. Consequently, the abrupt change between the

378 crystallization environment of the light-CL core and dark-CL rim is not due to the

379 magma mixing or contamination during magma evolution. Therefore, we propose that

380 the light-CL core was formed in a relatively deep magma chamber, which had low

381 oxygen fugacity, low Zr saturation and higher temperature. The low Th, U and REE,

382 and widely-spaced oscillatory zoning patterns indicate a low growth rate of zircon

383 (Hoskin and Schaltegger, 2003; Wang et al., 2011). In contrast, the dark-CL rim was

384 formed during the ascent and/or at the emplacement location of the magma. At this

stage, the oxygen fugacity significantly increased, the temperature decreased, and Zr saturation increased due to the crystallization differentiation. In this environment, the crystallization rate of zircon significantly increased, forming the zircons with a higher content of Th, U and REE elements, low CL emission and narrowly-spaced oscillatory zoning patterns.

Zircon U-Pb dating is the most commonly used method in geochronology, especially dating the emplacement age of magmatic rocks. A weighted mean age or upper intercept age is usually obtained to represent the emplacement time of a magmatic rock. However, the autocrystic zircons in this study record two different magmatic evolution stages. Previous studies, such as Wang et al. (2007), Zhao et al. (2014) and Chen et al. (2020), also show that zircons can crystallize continually or intermittently in a single phase of magmatism, showing several growth zones of clearly different internal structure and distinct time difference. Therefore, autocrystic zircon can be formed in two or more evolution stages during one distinct pulse or increment of magma. Some scholars even regard that the age difference of different stages can be more than dozens of Ma (Wang et al., 2007). Therefore, if the zircon ages in the same magmatic rock have a large range of variation, this could be caused by the zircons recording different stages in magmatic evolution, related to different levels of magma within the crust and/or different temperature regimes. In this paper, although the apparent age of the dark-CL rim is generally younger than that of the light-CL core, the age difference between the two is within the error range of the in-situ LA-ICP-MS analyses (individual spot of $\pm 3–5\%$ relative precision). Therefore, further work is

407 needed to verify the actual age difference between the two magmatic evolution stages.

408 Nevertheless, it is notable that the bulk petrology and geochemistry of the host pluton

409 does not record and reveal this two-stage magmatic evolution, which can only be

410 detected in the zircon analysis.

6.2 Genetic type: I-type affinity

412   The Zhoujiapuzi granite has low Zr (113 – 242 ppm), Ce (26.5 – 121.5 ppm),

413 Zr+Nb+Ce+Y (152.0 – 382.6 ppm), $(Na_2O + K_2O)/CaO$ (4.53 – 8.31) and FeO*/MgO

414 (5.09 – 10.56), distinct from the typical A-type granites (Fig. 11a-d). Furthermore, the

415 Zhoujiapuzi granite does not contain mafic alkaline minerals, such as arfvedsonite,

416 riebeckite, etc., which is also distinctly inconsistent with typical A-type granites (Wu et

417 al., 2003). Wu et al. (2017) suggested that a high formation temperature is one of the

418 most important characteristics of A-type granite. Zircon saturation thermometry (T_{Zrn})

419 and Ti-in-zircon thermometer (T_{Zr-Ti}) are two methods for estimating magma

420 temperatures. As noted above, because the values of $aSiO_2$ and $aTiO_2$ during the early

421 zircon crystallization cannot be accurately obtained, the temperature of this period

422 cannot be accurately obtained through the Ti-in-zircon thermometer. Zircon saturation

423 thermometry was introduced by Watson and Harrison (1983) and is suitable for non-

424 peralkaline crustal source rocks. Since the zircon solubility is mainly affected by

425 temperature, major element compositions have a limited impact on calculated T_{Zrn}

426 (Miller et al., 2003). In addition, the errors introduced by crystal-rich composition tend

427 to cancel as changes in Zr concentration and M value during crystallization have

428   opposite effects on the T_{zrn} value (Miller et al., 2003). Therefore, the composition of

429   Zhoujiapuzi granite can be used to estimate the magma temperature. The calculated T_{Zrn}

430   values for the Zhoujiapuzi granite are in the range of 803-870 °C (mean=845 ±20°C).

431   It was proposed that the T_{Zrn} suggests an upper limit on the temperature of melt

432   generation for inheritance-rich granitoid (Miller et al., 2003). Hence, the magma

433   temperature of the Zhoujiapuzi granite should be lower than or equal to the T_{Zrn} value,

434   which is significantly lower than that of typical A-type granite (>900 ℃, Skjerlie and

435   Johnston, 1992; Douce, 1997). Thus, the Zhoujiapuzi granite is not an A-type granite.

436   The samples of the Zhoujiapuzi granite have A/KNC < 1.1, relatively high Na_2O

437   (3.96–4.65 wt.%) and lack peraluminous minerals (e.g. cordierite, andalusite,

438   muscovite and garnet), which are clearly different from S-type granites (Chappell and

439   White, 1992). With the rise of the degree of crystallization, P_2O_5 contents

440   (generally>0.1 wt.%) increase in S-type granites, accompanied by an

441   increase/immutability in SiO_2 (Wolf and London, 1994). However, the Zhoujiapuzi

442   granite samples have low P_2O_5 contents (0.02－0.08 wt.%), and decrease with

443   increasing SiO_2 (Fig. 11e), which are features consistent with the I-type granite rather

444   than S-type granite (Chappell and White, 1992). Additionally, Rb has a positive

445   correlation with Y (Fig. 11f), which has been considered as an indicator of I-type granite

446   (Jiang et al., 2018). Furthermore, the composition of the Zhoujiapuzi granite fall in the

447   I-type granite field in the discrimination diagrams of granites introduced by Collins et

448   al. (1982) (Fig. 11 c-d). Therefore, we conclude that the Zhoujiapuzi granite is a I-type

449   granite.

6.3 Petrogenesis of the high Sr/Y granite

The samples of the Zhoujiapuzi granite have high Sr/Y and $(La/Yb)_N$ ratios and low Y and Yb contents (Fig. 12a) consistent with the geochemical signatures of modern adakites (Defant and Drummond, 1990). However, other geochemical parameters of the Zhoujiapuzi granite, such as the high K_2O/Na_2O ratio (0.93 –1.22), low Al_2O_3 content (14.49 –15.02%, except one) and Sr content (in half of the samples lower than 400 ppm), are obviously different from typical adakites ($K_2O/Na_2O \leqslant 0.42$, $Al_2O_3 \geqslant$ 15 %, Sr>400 ppm, Defant and Drummond., 1990; Drummond et al., 1996, Martin et al., 2005). A variety of petrogenetic models have been proposed for the origin of high Sr/Y magmatic rocks, such as partial melting of subducting oceanic crust (Model A, Defant and Drummond, 1990), delaminated lower continental crust (LCC) (Model B, Kay and Kay, 1993; Xu et al., 2002), differentiation of basaltic arc magma (Model C, Castillo et al., 1999), magma mixing between mantle-derived mafic and crust-derived silicic magmas (Model D, Ma et al., 2013a), partial melting of thickened basaltic LCC (Model E, Gao et al., 2004; Ou et al., 2017), or melting of a high Sr/Y (and La/Yb) source (Model F, Kamei et al., 2009; Ma et al., 2015).

6.3.1 Model A: Partial melting of subducting oceanic crust

The partial melting of the young, hot and hydrated subducted oceanic slab in the garnet stability field is the classical formation model of adakite (high Sr/Y rock) (Defant and Drummond, 1990). Studies have shown that the rock with this genetic model generally has the characteristics of high mantle components (such as MgO, CaO and Cr) because of the involvement of mantle magma (Wang et al., 2018). However, this phenomenon was not seen in the Zhoujiapuzi granite. In addition, the Zhoujiapuzi granite has high K_2O/Na_2O ratios (0.92–1.22, average 1.13), which is inconsistent with

the slab-derived adakites (K_2O/Na_2O= ~0.4, Martin et al., 2005). Moreover, the low εHf(t) values (-26.6 to -22.8) of the Zhoujiapuzi granite are also inconsistent with the magmas derived from the partial melting of oceanic crust, which generally have depleted isotopic character (Zhan et al., 2020). Furthermore, the Zhoujiapuzi granite has low Ti/Eu and high Nd/Sm radios (Fig. 13a), and markedly negative Nb-Ta anomalies (Fig. 4b), which are distinct from those of oceanic basalts (Yu et al., 2012). In summary, the Zhoujiapuzi granite is difficult to explain by Model A.

6.3.2 Model B: Delaminated lower continental crust (LCC)

High-density, garnet-bearing mafic lower crust delaminating or foundering into the asthenosphere mantle and subsequent interaction with mantle peridotite could produce high Sr/Y magmas (Kay and Kay 1993). Because the melt formed by partial melting of the delaminated lower crust would interact with mantle peridotite during magma ascent, the high Sr/Y magmas related to this petrogenetic model generally have high MgO, Mg# and TiO_2 (Gao et al., 2004; Ou et al., 2017; He et al., 2021). The MgO (0.10– 0.44 wt.%), Mg# (15– 26) and TiO_2 (0.09– 0.34 wt.%) values of Zhoujiapuzi granite are significantly lower than the above values (Fig. 13b- d). In addition, delamination of the lower crust generally occurs in within-plate extensional settings (Gao et al., 2004), and will form a large number of Mg-rich (Mg#>50) rocks due to the partial melting of lithospheric mantle and/or upwelling of asthenosphere (Ou et al., 2017). However, these Jurassic magmatic rocks in the Liaodong Peninsula are generally considered to be formed in a compressional environment related to the subduction of the Paleo-Pacific slab (Li et al., 2004; Yang et al., 2015a; Zhu and Xu, 2019; Zheng et al., 2018). Furthermore, the middle-late Jurassic granites are generally Mg-poor (Fig. 13c). Due to the high temperature of the asthenosphere (1200 °C, Parsons and

McKenzie, 1978; King et al., 2015), rocks formed by partial melting of the delaminated lower crust should possess a high-temperature fingerprint. T_{Zrn} has been used as a geothermometer to estimate partial melting temperatures (e.g., Miller et al., 2003; Collins et al., 2016). As mentioned before, the T_{Zrn} of the Zhoujiapuzi granite is below 900 °C, which is markedly lower than the temperature of the asthenosphere. Therefore, the petrogenetic model of delaminated lower continental crust (Model B) is also inconsistent with the Zhoujiapuzi granite.

6.3.3 Model C: Differentiation of basaltic arc magma

Low-pressure fractional crystallization (involving olivine + clinopyroxene + plagioclase + amphibole+ titanomagnetite) or high-pressure fractional crystallization (involving garnet) from basaltic magmas have been proposed as two ways to generate adakitic characteristics (Castillo et al., 1999; Macpherson et al., 2006).

However, the composition of the Zhoujiapuzi granite is relatively uniform, including SiO_2, MgO and Na_2O, which does not support major fractional crystallization (Xue et a., 2017). Furthermore, the Zhoujiapuzi granite has abundant inherited zircons and no obvious depletion of Sr, Eu and Ba, showing that this granite has not experienced extensive fractionation (Miller et al., 2003). The samples form clear partial melting trends on the La/Yb versus La diagram (Fig. 13e), which also suggests that partial melting was more important than fractional crystallization (Gao et al., 2007; Shahbazi et al., 2021). In addition, crystal fractionation of basaltic melts can only form minor volumes of granitic melts, the ratio of the two is about 9:1 (Zeng et al., 2016). However, for the same age interval, no coexisting mafic-intermediate rocks have been found in the research area. In the wider region of the Liaodong Peninsula, Middle-Late Jurassic magmatism is dominated by felsic compositions; mafic- intermediate rocks are only

reported in the Huaziyu area (lamprophyre dikes, Jiang et al., 2005). Therefore, it is

unlikely that there are large-scale mafic- intermediate rocks contemporaneous with the

Zhoujiapuzi granite at depth according to the rock assemblage of Liaodong Peninsula

in this period. Moreover, the zircon Hf isotopic compositions of the Zhoujiapuzi granite

are quite different from those of the depleted mantle, but are similar to those of the

basement (Liaohe Group and Liaoji granite) in the study area (Fig. 8). The ancient

inherited zircons (2500 to 2173) with low $\varepsilon Hf(t)$ values also indicate older crustal

material in the Zhoujiapuzi granite. For these reasons, it is highly improbable that

Zhoujiapuzi granite was derived by differentiation of basaltic magma (Model C).

6.3.4 Model D: Magma mixing between mantle-derived mafic and crust-derived silicic magmas

The Zhoujiapuzi granite has high K_2O/Na_2O ratio (>1) and A/CNK value (>1),

together with the absence of mingling textures, mafic microgranular enclaves (MMEs),

felsic xenocrysts and melting texture of plagioclase, implying that the mantle-derived

magma is unlikely to have played an important role in the genesis of the Zhoujiapuzi

granite (Castro et al., 1991). In addition, the Zhoujiapuzi granite is characterized by the

development of biotite, but lacks amphibole and pyroxene. These features, coupled with

the high A/CNK value, are consistent with an origin as a crust-derived granitoid, but

obviously different from the granitoids formed by crust-mantle-derived magma mixing

(Barbarin, 1990). Moreover, granites formed by magma mixing generally have high

MgO, TFe_2O_3, CaO and Cr contents and low SiO_2 content (Ma et al., 2013a; Wang et

al., 2018). These features are obviously inconsistent with the Zhoujiapuzi granite in this

study. Additionally, the $\varepsilon Hf(t)$ values and trace element composition of the two stages

of zircon also do not support magma mixing. Hence, magma mixing of mantle-derived

546 and crust-derived magmas (Model D) is also unlikely to have produced the Zhoujiapuzi

547 granite.

6.3.5 Model E: Partial melting of thickened basaltic LCC

549   Experimental studies have shown that the partial melt of basaltic LCC in the garnet

550 stabilization zone (> 40 km, i.e. ~1.2 GPa) can produce magma with a high Sr/Y ratio

551 (Rapp et al., 2003 and references therein). In these scenarios, high Sr/Y and overall

552 adakitic affinity are caused by leaving garnet as residual phases (e.g. Gao et al., 2004).

553 Based on geochemical data for the Zhoujiapuzi granites, partial melting of thickened

554 basaltic LCC is also unlikely to account for the high Sr/Y Zhoujiapuzi granite (Model

555 E). This conclusion is based on the following observations:

556   (1) This ratio of $(Gd/Yb)_N$ is the most important feature to judge whether garnet is

557 involvement in magma genesis (Ma et al., 2012). If the $(Gd/Yb)_N$ ratio of the source is

558 similar to the average value of the LCC (1.71, Rudnick and Gao, 2003), partial melting

559 of these crustal materials controlled by garnet at high pressure can produce melt with

560 $(Gd/Yb)_N$ of 5.8 (Huang and He, 2010). In contrast, the $(Gd/Yb)_N$ values (1.22–5.06,

561 average 2.69) of the Zhoujiapuzi granite are relatively low. (2) Studies of lower-crustal

562 xenoliths show that garnet may not be a common mineral in the lower crust of the NCC

563 (Ma et al., 2012). (3) As shown in the discrimination diagrams of granite sources (Fig.

564 13f, g), all samples fall in the range of metagreywacke-derived melts. Therefore, the

565 Zhoujiapuzi granite was considered to have been derived from crustal anatexis of

566 metagraywacke (or intermediate-acid igneous rock with similar mineral composition),

567 rather than basaltic lower crust.

6.3.6 Model F: Melting of a high Sr/Y (and La/Yb) source

Studies have shown that when a source rock has a high Sr/Y ratio, the high Sr/Y signature of the derived magma can inherit from their source, regardless of pressure (Kamei et al., 2009; Moyen, 2009; Ma et al., 2015). We suggest that partial melting of high Sr/Y Liaoji granite was most probably the origin of the high Sr/Y Zhoujiapuzi granite, as discussed below (Model F).

The Zhoujiapuzi granite has similar mineral assemblages (contains abundant K-feldspar and lacks hornblende) and geochemical composition (Fig. 13h) to the Tsutsugatake intrusion, which is explained by partial melting of arc-type tonalite or adakitic granodiorite (Kamei et al., 2009). Among the inherited zircons from Zhoujiapuzi granite, the ^{207}Pb / ^{206}Pb ages of all the spots are between 2132 and 2200 Ma, except one, and yield a Concordia upper intercept age of 2163 Ma. Both assimilation of country-rocks and incomplete melting of source rocks can explain the genesis of inherited zircon in granite. Due to the similar T_{DM2} of autocrystic zircons (light-CL core and dark-CL rim) and inherited zircons, these inherited zircons most likely come from the source of the Zhoujiapuzi granite. In the study area, meta-sedimentary rocks and meta-volcanic rocks of the South Liaohe Group, Paleoproterozoic mafic rocks, as well as the Liaoji granites, have ~2.16 Ga zircon. In spite of an age peak of 2.17–2.16 Ga in detrital zircon age spectra of the metasediments from the South Liaohe Group, melting of a sediment-dominated source is unlikely to have occurred, as it would have also introduced other age peaks such as ~2.03 Ga and ~2.50 Ga (Li et al., 2015; Wang et al., 2020b). In addition, given the I-type characteristics of the Zhoujipuzi granite, derivation from an igneous precursor is more plausible rather than a metasedimentary origin (Chappell and White, 1992). Therefore, these ~2.16 Ga zircons from the Zhoujiapuzi granite are unlikely to come from the

South Liaohe Group. As shown in the host rock discrimination diagrams (Fig. 14, introduced by Belousova et al., 2002), all the ~2.16 Ga inherited zircons from Zhoujiapuzi granite fall into the granitoid area (Fig. 14), precluding that these ~2.16 Ga zircon come from the Paleoproterozoic mafic rocks. In addition, the ~2.16 Ga inherited zircons from Zhoujiapuzi granite and the zircons from the Liaoji granites lie in a similar area in the εHf(t)-age (Ma) diagram (Fig. 8). Hence, the ~2.16 Ga inherited zircon most likely come from the Liaoji granites.

Some of the Liaoji granites, such as the Muniuhe granite (comprising granodiorite and syenogranite with no distinct boundary between the two), have adakitic signatures, and similar REE and trace element patterns as the Zhoujiapuzi granite (Fig. 4). Based on a model of batch melting (Shaw, 1970) using the experiments of Conrad et al. (1988), the high Sr/Y characteristic of the Zhoujiapuzi granite can be explained by partial melting of Muniuhe granitic pluton leaving amphibole as the main residue (Fig. 12b).

In our modelling, we choose the XY-005 sample to approximately represent the primitive melt composition. The reasons are as below: as mentioned above, the high Sr/Y characteristics of the Zhoujiapuzi granite are not caused by the fractional crystallization of amphibole. Furthermore, the lack of positive correlation between Dy_N/Yb_N ratios and La_N/Yb_N ratios (Fig. 13i) also suggests that fractional crystallization of amphibole was not a significant process for the Zhoujiapuzi granite. On the other hand, the samples of Zhoujiapuzi granite display variable Eu and Sr contents, implying that plagioclase is likely a fractional phase. The separation of titanomagnetite could explain the positive trend in TFe_2O_3 with increasing TiO_2 content, consistent with the occurrences of magnetite in some studied rocks. This possible mineral assemblage of fractional crystallization is also reflected by the chemical variations in the Sr/Y-Y diagram (Fig. 12b). Hence, the sample XY-005, which has

highest Sr/Y, was chosen to represent a primitive melt composition. To find the best matching experimental melts, we have compared the major elements of the XY-005 sample with that of experimental melts and the characteristics of no garnet residue discussed above. Results are shown in Fig. 12b. The Sr and Y compositions of the starting material used in these experiments resemble those of the average composition of the Muniuhe granitic pluton (Sr=475 ppm, Y=9.77 ppm), if the residue contains a large volume of amphibole (>90 %). However, if more plagioclase is retained in the residue (e.g. 18.3 %), a source region with a higher Sr content is required. Therefore, a similar high Sr/Y Liaoji granite to the Muniuhe granitic pluton can produce the high Sr/Y signatures of the Zhoujiapuzi granite.

A large number of Yanshanian adakites (or high Sr/Y rocks) are developed in the NCC, which are generally considered to be derived from the thickened basaltic LCC (e.g. Gao et al., 2004; Wu et al., 2005a; Ma et al., 2013b). Zhang et al. (2001, 2003) suggested that these so-called "C-type adakites" indicated a large-scale crustal thickening event. However, according to the studies on the Triassic and Jurassic adakitic rocks near the Pingquan area, the northern part of the NCC, Ma et al. (2012, 2015) suggested that the adakitic signatures of these rocks are inherited from their source rocks. The research of the Zhoujiapuzi granite in this study also shows that among the widely distributed Jurassic high Sr/Y granites in the Liaodong Peninsula, there is at least one pluton with a high Sr/Y signature inherited from the source. Therefore, we suggest that melting of a high Sr/Y (and La/Yb) source is one of the important processes for the generation of Yanshanian high Sr/Y rocks in the NCC. This kind of high Sr/Y granite does not need to be formed in the garnet stability field.

6.4 Tectonic implications

A large number of Early Jurassic arc-like igneous rocks occur in the northeast part of NCC- Korean Peninsula-Hida belt, which belong to the middle-high K calc-alkaline series and are characterized by enrichment in LILE and depletions in HFSE (Wu et al., 2007; Tang et al., 2018 and references therein). In addition, the Early Jurassic accretionary complexes in the eastern margin of the Eurasian continent and the Japan islands, such as the Heilongjiang complex, the Khabarovsk complex and the Mino-Tamba complex, are considered to be related to subduction (Wu et al., 2007; Tang et al., 2018 and references therein). It is generally accepted that the Paleo-Pacific slab subducted westwards in the Early Jurassic (Tang et al., 2018; Zhu and Xu, 2018).

In the middle-late Jurassic, I-type granites are dominant in the Liaodong Peninsula, such as the Zhoujiapuzi granite (this study), Heigou pluton, Gaoliduntai pluton (Wu et al., 2005a), Waling granite (Yang et al., 2015a) and Wulong granite (Yang et al., 2018). There are not A-type granites, and mantle derived magmatism is extremely rare. These granites were formed by partial melting of crustal materials without obvious contribution of mantle derived magma (Wu et al., 2005a; Yang et al., 2015b, 2018; Xue et al., 2020). In addition, WNW-ESE compression during 157-143 Ma was widespread in the Liaodong Peninsula (Yang et al., 2004; Zhang et al., 2020). It not only mylonitized the granite plutons in middle-lower crust levels, but also intensely deformed the thick sedimentary cover in the upper crust (Qiu et al., 2018; Ren et al., 2020). Hence, Late Jurassic magmatism in the Liaodong peninsula is most likely to be related to subduction of the Paleo-Pacific plate in a mature continental arc, with crust

663   previously thickened by compressional tectonics, related to both the oceanic subduction

664   and the earlier Mesozoic collisions at the north and south margins of the NCC. This

665   setting would produce the conditions required for extensive crustal melting of pre-

666   existing basement. There is a potential resemblance to the modern arc of the Central

667   Andes (Allmendinger et al., 1997), where crustal thickening and plateau growth has

668   developed over the Cenozoic (Scott et al., 2018), and melting of older basement has

669   taken place during subduction of the Nazca plate (Miller and Harris, 1989). This model

670   is also consistent with the idea that much of eastern China was a high orogenic plateau

671   during the Mesozoic, before widespread Early Cretaceous extension and core complex

672   development (Meng, 2003; Chu et al., 2020).

673   **7. Conclusions**

674   (1) LA-ICP-MS zircon U-Pb dating indicates that the Zhoujiapuzi granite in the

675   Liaodong Peninsula formed at ~160 Ma.

676   (2) Zircon growth in Zhoujiapuzi granite can be divided into two distinct stages.

677   The light-CL core was formed in a deeper, hotter, magma chamber, which had low

678   oxygen fugacity and high temperature. The dark-CL rim formed from later, more

679   evolved, magma. Oxygen fugacity significantly increased and the temperature

680   decreased at this stage. The Zhoujiapuzi granite is a case study of multistage generation

681   and emplacement of magma, revealed by zircons, where no signals are discernible in

682   the bulk petrology or geochemistry.

683   (3) The I-type Zhoujiapuzi granite originated from partial melting of the

684 Paleoproterozoic Liaoji granites. The high Sr/Y compositions are inherited from their

685 source rocks, rather than being a direct indication of deep crustal melting, or any other

686 common mechanism for generating adakitic signatures.

687 (4) The Late Jurassic tectonic setting of the Liaodong Peninsula and the eastern

688 NCC resembled the modern orogenic plateau of the Central Andes, where silicic

689 magmatism may occur by partial melting of older continental crust in a compressional

690 environment, related to the subduction of the Paleo-Pacific plate.

701 **References**

702 Allmendinger, R. W., Jordan, T. E., Kay, S. M., and Isacks, B. L.: The evolution of the

703 Altiplano-Puna plateau of the Central Andes, Annu. Rev. Earth Pl. Sc., 25, 139–

704 174, https://doi.org/10.1146/annurev.earth.25.1.139, 1997.

705   Altherr, R., Holl, A., Hegner, E., Langer, C. and Kreuzer, H.: High-potassium, calc-

706   alkaline I-type plutonism in the European Variscides: northern Vosges (France)

707   and northern Schwarzwald (Germany), Lithos, 50(1-3), 51–73,

708   https://doi.org/10.1016/S0024-4937(99)00052-3, 2000.

709   Ballard, J. R., Palin, M. J., and Campbell, I. H.: Relative oxidation states of magmas

710   inferred from Ce(IV)/Ce(III) in zircon: application to porphyry copper deposits of

711   northern Chile. Contrib. Mineral. Petrol., 144, 347–364,

712   https://doi.org/10.1007/s00410-002-0402-5, 2002.

713   Barbarin, B.: Granitoids: main petrogenetic classifification in relation to origin and

714   tectonic setting, Geol. J., 25, 227–238, 1990.

715   Belousova, E., Griffin, W., O'Reilly, S. Y., and Fisher, N.: Igneous zircon: trace

716   element composition as an indicator of source rock type, Contrib. Mineral. Petrol.,

717   143, 602–622, https://doi.org/10.1007/s00410-002-0364-7, 2002.

718   Blichert-Toft, J., and Albarède, F.: The Lu-Hf isotope geochemistry of chondrites and

719   the evolution of the mantle-crust system, Earth. Planet. Sc. Lett., 148(1), 243–258,

720   https://doi.org/10.1016/S0012-821X(97)00040-X, 1997.

721   Breiter, K., Lamarão, C. N., Borges, R. M. K., and Dall'Agnol, R.: Chemical

722   characteristics of zircon from A-type granites and comparison to zircon of S-type

723   granites, Lithos, 192–195, 208–225, https://doi.org/10.1016/j.lithos.2014.02.004,

724   2014.

725   Castillo, P. R., Janney, P. E., and Solidum, R. U.: Petrology and geochemistry of

726   Camiguin Island, southern Philippines: Insights to the source of adakites and other

lavas in a complex arc setting, Contrib. Mineral. Petrol., 134(1), 33–51, https://doi.org/10.1007/s004100050467, 1999.

Castro, A., Moreno-Ventas, I., and Rosa, J.: H-type (hybrid) granitoids: a proposed revision of the granite-type classification and nomenclature, Earth. Sci. Rev., 31, 237–253, https://doi.org/10.1016/0012-8252(91)90020-G, 1991.

Chappell, B. W., and White, A. J. R.: I-and S-type granites in the Lachlan Fold Belt, Geol. Soc. Am. Spec. Pap., 272, 1–26, https://doi.org/10.1130/SPE272-p1, 1992.

Chen, S. R., Wang, Q., Zhu, D. C., Weinberg, R. F., Zhang, L. L., and Zhao, Z. D.: Reheating and magma mixing recorded by zircon and quartz from high-silica rhyolite in the Coqen region, southern Tibet, Am. Miner., https://doi.org/10.2138/am-2020-7426, 2020.

Chu, Y., Lin, W., Faure, M., Allen, M. B., and Feng, Z.: Cretaceous exhumation of the Triassic intracontinental Xuefengshan Belt: Delayed unroofing of an orogenic plateau across the South China Block? Tectonophysics, 793, 228592, https://doi.org/1016/j.tecto.2020.228592, 2020.

Claiborne, L. L., Miller, C. F., Walker, B. A., Wooden, J. L., Mazdab, F. K., and Bea, F.: Tracking magmatic processes through Zr/Hf ratios in rocks and Hf and Ti zoning in zircons: An example from the Spirit Mountain batholith, Nevada. Mineral. Mag., 70, 517–543, https://doi.org/10.1180/0026461067050348, 2006.

Collins, W. J., Beams, S. D., White, A. J. R., and Chappell, B. W.: Nature and origin of A-type granites with particular reference to southeastern Australia, Contrib. Mineral. Petr., 80, 189-200, https://doi.org/10.1007/BF00374895, 1982.

749 Collins, W. J., Huang, H. Q., and Jiang, X. Y.: Water-fluxed crustal melting produces

750 Cordilleran batholiths, Geology, 44(2), 143–146,

751 https://doi.org/10.1130/G37398.1, 2016.

752 Conrad, W. K., Nicholls, I. A., and Wall, V. J.: Water-saturated and -undersaturated

753 melting of metaluminous and peraluminous crustal compositions at 10 kb:

754 evidence for the origin of silisic magmas in the Taupo Volcanic Zone, New

755 Zealand, and other occurrences, J. Petrol., 29, 765–803,

756 https://doi.org/10.1093/petrology/29.4.765, 1988.

757 Defant, M. J., and Drummond, M. S.: Derivation of some modern arc magmas by

758 melting of young subducted lithosphere, Nature, 347, 662–665,

759 https://doi.org/10.1038/347662a0, 1990.

760 Douce, A. E. P.: Generation of metaluminous A-type granites by low-pressure melting

761 of calc-alkaline granitoids, Geology, 25, 743–746, https://doi.org/10.1130/0091-

762 7613(1997)025<0743:GOMATG>2.3.CO;2, 1997.

763 Drummond, M. S., Defant, M. J., and Kepezhinskas, P. K.: Petrogenesis of slab-derived

764 trondhjemite–tonalite–dacite/adakite magmas, Trans. R. Soc. Edinb., 87, 205–215,

765 https://doi.org/10.1017/S0263593300006611, 1996.

766 Faure, M., Lin, W., Moni, P., and Bruguier, O.: Paleoproterozoic arc magmatism and

767 collision in Liaodong Peninsula, NE China, Terra. Nova., 16, 75–80,

768 https://doi.org/10.1111/j.1365-3121.2004.00533.x, 2004.

769 Ferry, J. M., and Watson, E. B.: New thermodynamic models and revised calibrations

770 for the Ti-in-zircon and Zr-in-rutile thermometers, Contrib. Mineral. Petrol., 154,

429–437, https://doi.org/10.1007/s00410-007-0201-0, 2007.

Frost, B. R., Barnes, C. G., Collins, W. J., Arculus, R. J., Ellis, D. J., and Frost, C. D.: A geochemical classification for granitic rocks, J. Petrol., 42, 2033–2048, https://doi.org/10.1093/petrology/42.11.2033, 2001.

Gao, S., Rudnick, R. L., Yuan, H. L., Liu, X. M., Liu, Y. S., Xu, W. L., Ling, W. L., Ayers, J. C., Wang, X. C., and Wang, Q. H.: Recycling lower continental crust in the North China craton, Nature, 432, 892–897, https://doi.org/10.1038/nature03162, 2004.

Gao, Y. F., Hou, Z. Q., Kamber, B. S., Wei, R. H., Meng, X.J., and Zhao, R. S.: Adakite-like porphyries from the southern Tibetan continental collision zones: evidence for slab melt metasomatism, Contrib. Mineral. Petr., 153, 105–20, 10.1007/s00410-006-0137-9, 2007.

Griffin, W. L., Belousova, E. A., Shee, S. R., Pearson, N. J., and O'Reilly, S. Y.: Archean crustal evolution in the northern Yilgarn Craton: U-Pb and Hf-isotope evidence from detrital zircons, Precambrian. Res., 131, 231–282, https://doi.org/10.1016/J.PRECAMRES.2003.12.011, 2004.

He, P. L., Huang, X. L., Yang, F., and Wang, X.: Mineralogy constraints on magmatic processes controlling adakitic features of Early Permian high-magnesium diorites in the Western Tianshan orogenic belt, J. Petrol., 61, a114, https://doi.org/10.1093/petrology/egaa114, 2021.

Hoskin, P. W. O.: Trace-element composition of hydrothermal zircon and the alteration of Hadean zircon from the Jack Hills, Australia, Geochim. Cosmochim. Ac., 69,

637–648, https://doi.org/10.1016/j.gca.2004.07.006, 2005.

Hoskin, P. W., and Schaltegger, U.: The composition of zircon and igneous and metamorphic petrogenesis, Rev. Mineral. Geochem., 53, 27–62, https://doi.org/10.2113/0530027, 2003.

Huang, F., and He, Y.S.: Partial melting of the dry mafic continental crust: Implications for petrogenesis of C-type adakites, Chinese. Sci. Bull., 55, 1255–1267, https://doi.org/10.1007/s11434-010-3224-2, 2010.

Jackson, S. E., Pearson, N. J., Griffin W L, and Belousova, E. A.: The application of laser ablation-inductively coupled plasma-mass spectrometry to in situ U-Pb zircon geochronology, Chem. Geol., 211(1-2), 47–69, https://doi.org/doi:10.1016/j.chemgeo.2004.06.017, 2004.

Jiang, H., Jiang, S. Y., Li, W. Q., Zhao, K. D., and Peng, N. J.: Highly fractionated Jurassic I-type granites and related tungsten mineralization in the Shirenzhang deposit, northern Guangdong, South China: Evidence from cassiterite and zircon U-Pb ages, geochemistry and Sr-Nd-Pb-Hf isotopes, Lithos, S480187509, https://doi.org/10.1016/j.lithos.2018.04.030, 2018.

Jiang, Y.H., Jiang, S.Y., Zhao, K.D., Ni, P., Ling, H.F., and Liu, D.Y.: SHRIMP U-Pb zircon dating for lamprophyre from Liaodong Peninsula: Constraints on the initial time of Mesozoic lithosphere thinning beneath eastern China, Chinese. Sci. Bull., 50, https://doi.org/10.1360/982005-373, 2612–2620, 2005.

Kamei, A., Miyake, Y., Owada, M., and Kimura, J.: A pseudo adakite derived from partial melting of tonalitic to granodioritic crust, Kyushu, southwest Japan arc,

Lithos, 112, 615–625, https://doi.org/10.1016/j.lithos.2009.05.024, 2009.

Kay, R. W., and Kay, S. M.: Delamination and delamination magmatism, Tectonophysics, 219, 177–189, https://doi.org/10.1016/0040-1951(93)90295-U, 1993.

King, S. D., Frost, D. J., and Rubie D. C.: Why cold slabs stagnate in the transition zone, Geology, 43(3), 231–234, https://doi.org/10.1130/G36320.1, 2015.

Li, C.M., Zhang, C.H., Cope, T.D., and Lin, Y.: Out-of-sequence thrusting in polycyclic thrust belts: An example from the Mesozoic Yanshan belt, North China Craton, Tectonics, 35, 2082–2116, https://doi.org/10.1002/2016TC004187, 2016.

Li, S. Z., and Zhao, G. C.: SHRIMP U-Pb zircon geochronology of the Liaoji granitoids: Constraints on the evolution of the Paleoproterozoic Jiao-Liao-Ji belt in the Eastern Block of the North China Craton, Precambrian. Res., 158, 1–16, https://doi.org/10.1016/j.precamres.2007.04.001, 2007.

Li, S. Z., Zhao, G. C., Sun, M., Han, Z. Z., Hao, D. F., Luo, Y., and Xia, X. P.: Deformation history of the Paleoproterozoic Liaohe Group in the Eastern Block of the North China Craton, J. Asian. Earth. Sci., 24, 659–674, https://doi.org/659–67410.1016/j.jseaes.2003.11.008, 2005.

Li, S.Z., Liu, J.Z., Zhao, G.C., Wu, F.Y., Han, Z.Z., and Yang, Z.Z.: Key geochronology of Mesozoic deformation in the eastern block of the North China Craton and its constraints on regional tectonics: A case of Jiaodong and Liaodong Peninsula, Acta. Petrol. Sin., 2, 633–646, https://doi.org/10.1007/BF02873097, 2004.

Li, X.H., Long, W.G., Li, Q.L., Liu, Y., Zheng, Y.F., Yang, Y.H., Chamberlain, K.R., Wan, D.F., Guo, C.H., and Wang, X.C.: Penglai Zircon Megacrysts: A Potential New Working Reference Material for Microbeam Determination of Hf-O Isotopes and U-Pb Age, Geostand. Geoanal. Res., 34, 117–134, https://doi.org/info:doi/10.1111/j.1751-908X.2010.00036.x, 2010.

Li, Z., Chen, B., Liu, J.W., Zhang, L., and Yang, C.: Zircon U-Pb ages and their implications for the South Liaohe Group in the Liaodong Peninsula, Northeast China (in Chinese with English abstract), Acta. Petrol. Sin., 31(6), 1589–1605, 2015.

Liu, Y.S., Hu, Z.C., Zong, K.Q., Gao, C.G., Gao, S., Xu, J., and Chen, H.H.: Reappraisement and refinement of zircon U-Pb isotope and trace element analyses by LA-ICP-MS, Chinese. Sci. Bull., 55, 1535–1546, https://doi.org/10.1007/s11434-010-3052-4, 2010.

Loader, M. A., Wilkinson, J. J., and Armstrong, R. N.: The effect of titanite crystallisation on Eu and Ce anomalies in zircon and its implications for the assessment of porphyry Cu deposit fertility, Earth. Planet. Sc. Lett., 472, 107–119, https://doi.org/10.1016/j.epsl.2017.05.010, 2017.

Ludwig, K. R.: User's manual for Isoplot 3.00: a geochronological toolkit for Microsoft Excel, Berkeley. Geochronology. Center., 2003.

Ma, L., Jiang, S.Y., Dai, B.Z., Jiang, Y.H., Hou, M.L., Pu, W., and Xu, B.: Multiple sources for the origin of Late Jurassic Linglong adakitic granite in the Shandong Peninsula, eastern China: Zircon U-Pb geochronological, geochemical and Sr-Nd-

Hf isotopic evidence, Lithos, 162–163, 251–263, https://doi.org/10.1016/j.lithos.2013.01.009, 2013b.

Ma, Q., Zheng, J.P., Griffin, W. L., Zhang, M., Tang, H.Y., Su, Y.P., and Ping, X.Q.: Triassic "adakitic" rocks in an extensional setting (North China): Melts from the cratonic lower crust, Lithos, 149, 159–173, https://doi.org/10.1016/j.lithos.2012.04.017, 2012.

Ma, Q., Zheng, J.P., Xu, Y.G., Griffin, W. L., and Zhang, R.S.: Are continental "adakites" derived from thickened or foundered lower crust? Earth. Planet. Sc. Lett., 419, 125–133, https://doi.org/10.1016/j.epsl.2015.02.036, 2015.

Ma, X.H., Chen, B., and Yang, M.C.: Magma mixing origin for the Aolunhua porphyry related to Mo-Cu mineralization, eastern Central Asian Orogenic Belt, Gondwana. Res., 24, 1152–1171, https://doi.org/10.1016/j.gr.2013.02.010, 2013a.

Macpherson, C. G., Dreher, S. T., and Thirlwall, M. F.: Adakites without slab melting: High pressure differentiation of island arc magma, Mindanao, the Philippines, Earth. Planet. Sc. Lett., 243(3), 581–593, https://doi.org/10.1016/j.epsl.2005.12.034, 2006.

Mahon, K. I.: The New "York" regression: Application of an improved statistical method to geochemistry, Int. Geol. Rev., 38(4), 293–303, https://doi.org/10.1080/00206819709465336, 1996.

Maniar, P. D., and Piccoli, P. M.: Tectonic discrimination of granitoids, Geol. Soc. Am. Bull., 101, 635–643, https://doi.org/10.1130/0016-7606(1989)101<0635:TDOG>2.3.CO;2, 1989.

Martin, H., Smithies, R.H., Rapp, R., Moyen, J.-F., and Champion, D.: An overview of adakite, tonalite-trondhjemite-granodiorite (TTG), and sanukitoid: relationships and some implications for crustal evolution, Lithos, 79, 1–24, https://doi.org/10.1016/j.lithos.2004.04.048, 2005.

Meng, E., Liu, F.L., Liu, P.H., Liu, C.H., Yang, H., Wang, F., Shi, J.R., and Cai, J.: Petrogenesis and tectonic significance of Paleoproterozoic meta-mafic rocks from central Liaodong Peninsula, northeast China: Evidence from zircon U-Pb dating and in situ Lu-Hf isotopes, and whole-rock geochemistry, Precambrian. Res., 247, 92–109, https://doi.org/10.1016/j.precamres.2014.03.017, 2014.

Meng, Q. R.: What drove late Mesozoic extension of the northern China-Mongolia tract? Tectonophysics, 369, 155–174, https://doi.org/0.1016/S0040-1951(03)00195-1, 2003.

Mezger, K., and Krogstad, E. J.: Interpretation of discordant U-Pb zircon ages: An evaluation, J. Metamorph. Geol., 15, 127–140, https://doi.org/10.1111/j.1525-1314.1997.00008.x,1997.

Miller, C. F., McDowell, S. M., and Mapes, R. W.: Hot and cold granites? Implications of zircon saturation temperatures and preservation of inheritance, Geology, 31, 529–532, https://doi.org/10.1130/0091-7613(2003)031<0529:hacgio>2.0.co;2, 2003.

Miller, J.F., and Harris, N.B.W.: Evolution of continental crust in the Central Andes; constraints from Nd isotope systematics, Geology, 17, 615–617, https://doi.org/10.1130/0091-7613(1989)0172.3.CO;2, 1989.

903 Moyen, J.: High Sr/Y and La/Yb ratios: The meaning of the "adakitic signature", Lithos,

904   112, 556–574, https://doi.org/10.1016/j.lithos.2009.04.001, 2009.

905 Nakamura, H., and Iwamori, H.: Generation of adakites in a cold subduction zone due

906   to double subducting plates, Contrib. Mineral. Petr., 165, 1107–1134,

907   https://doi.org/10.1007/s00410-013-0850-0, 2013.

908 Nasdala, L., Pidgeon, R. T., Wolf, D., and Irmer, G., Metamictization and U-Pb isotopic

909   discordance in single zircons: a combined Raman microprobe and SHRIMP ion

910   probe study, Miner. Petrol., 62, 1–27, https://doi.org/10.1007/BF01173760, 1998.

911 Nash, D.J., Ciborowski, T., Ullyott, J.S., Pearson, M.P. and Whitaker, K.A.: Origins of

912   the sarsen megaliths at Stonehenge, Sci. Adv., 6, eabc0133,

913   https://doi.org/10.1126/sciadv.abc0133, 2020.

914 Ou, Q., Wang, Q., Wyman, D. A., Zhang, H.X., Yang, J.H., Zeng, J.P., Hao, L.L., Chen,

915   Y.W., Liang, and H., Qi, Y.: Eocene adakitic porphyries in the central-northern

916   Qiangtang Block, central Tibet: Partial melting of thickened lower crust and

917   implications for initial surface uplifting of the plateau, J. Geophys. Res. Solid.

918   Earth., 122, 1025–1053, https://doi.org/10.1002/2016JB013259, 2017.

919 Parsons, B., and Dan, M.K.: Mantle convection and the thermal structure of the plates,

920   J. Geophys. Res. Solid. Earth., 83, https://doi.org/10.1029/JB083iB09p04485,

921   1978.

922 Patiño Douce, A.E.P.: What do experiments tell us about the relative contributions of

923   crust and mantle to the origin of granitic magmas? Geol. Soc. Lond. Spec. Publ.,

924   168(1), 55–75, https://doi.org/10.1144/GSL.SP.1999.168.01.05, 1999.

Qiu, L., Kong, R.Y., Yan, D.P., Wells, M.L., Wang, A.P., Sun, W.H., Yang, W.X., Han,

Y.G., Li, C.M., and Zhang, Y.X.: The Zhayao tectonic window of the Jurassic

Yuantai thrust system in Liaodong Peninsula, NE China: Geometry, kinematics

and tectonic implications, J. Asian Earth Sci., 164, 58–71, https://doi.org/

10.1016/j.jseaes.2018.06.012, 2018.

Rapp, R. P., Shimizu, N and Norman, M.D.: Growth of early continental crust by partial

melting of eclogite, Nature, 425(6958), 605–609,

https://doi.org/10.1038/nature02031, 2003.

Ren, Z.H., Lin, W., Faure, M., Meng, L.T., Qiu, H.B., and Zeng, J.P.: Triassic- Jurassic

evolution of the eastern North China Craton: Insights from the Lushun-Dalian area,

South Liaodong Peninsula, NE China, Geol. Soc. Am. Bull., 133(1–2),

https://doi.org/10.1130/B35533.1, 2020.

Rudnick, R. L., and Gao, S.: Composition of the continental crust, Treatise. Geochem.,

3, 1–64, https://doi.org/10.1016/b0-08-043751-6/03016-4, 2003.

Schiller, D., and Finger, F.: Application of Ti-in-zircon thermometry to granite studies:

problems and possible solutions, Contrib. Mineral. Petr., 174,

https://doi.org/10.1007/s00410-019-1585-3, 2019.

Schmitz, M. D., and Kuiper, K. F.: High-Precision Geochronology, Elements., 9, 25–

30, https://doi.org/10.2113/gselements.9.1.25, 2013.

Schwartz, J. J., Johnson, K., Miranda, E. A., and Wooden, J. L.: The generation of high

Sr/Y plutons following Late Jurassic arc–arc collision, Blue Mountains province,

NE Oregon, Lithos, 126, 22–41, https://doi.org/10.1016/j.lithos.2011.05.005,

947   2011.

948 Scott, E.M., Allen, M.B., Macpherson, C.G., McCaffrey, K.J.W., Davidson, J.P.,

949   Saville, C., and Ducea, M.N.: Andean surface uplift constrained by radiogenic

950   isotopes of arc lavas, Nat. Commun., 9(1), 969, https://doi.org/10.1038/s41467-

951   018-03173-4, 2018.

952 Shahbazi, H., Maghami, Y. T., Azizi, H., Asahara, Y., Siebel, Y., Maanijou, M., and

953   Rezai, A.: Zircon U-Pb ages and petrogenesis of late Miocene adakitic rocks from

954   the Sari Gunay gold deposit, NW Iran, Geol. Mag.,

955   https://doi.org/10.1017/S0016756821000297, 2021.

956 Shannon. R.D.: Revised effective ionic radii and systematic studies of interatomic

957   distances in halides and chalcogenides, Acta. Crystall. A., 32(5), 751–767,

958   https://doi.org/10.1107/S0567739476001551, 1976.

959 Shaw, D.M.: Trace element fractionation during anatexis, Geochim. Cosmochim. Ac.,

960   34, 237–243, https://doi.org/10.1016/0016-7037(70)90009-8, 1970.

961 Siégel, C., Bryan, S. E., Allen, C. M., and Gust, D. A.: Use and abuse of zircon-based

962   thermometers: A critical review and a recommended approach to identify

963   antecrystic zircons, Earth. Sci. Rev., 176, 87–116,

964   https://doi.org/10.1016/j.earscirev.2017.08.011, 2018.

965 Skjerlie, K. P., and Johnston, A. D.: Vapor-absent melting at 10 kbar of a biotite-and

966   amphibole-bearing tonalitic gneiss: implications for the generation of A-type

967   granites, Geology, 20, 263–266, https://doi.org/10.1130/0091-

968   7613(1992)0202.3.CO;2, 1992.

Sláma, J., Košler, J., and Condon, D. J.: Plešovice zircon-A new natural reference material for U-Pb and Hf isotopic microanalysis, Chem. Geol., 249(1–2), 1–35, https://doi.org/doi:10.1016/j.chemgeo.2007.11.005, 2008.

Söderlund, U., Patchett, P.J., Vervoort, J.D., and Isachsen, C.E.: The 176 Lu decay constant determined by Lu-Hf and U-Pb isotope systematics of Precambrian mafic intrusions, Earth. Planet. Sc. Lett., 219(3), 311–324, https://doi.org/10.1016/S0012-821X(04)00012-3, 2004.

Sun, S. S., and McDonough, W. F.: Chemical and isotopic systematics of oceanic basalts: implications for mantle composition and processes, Geol. Soc. Lond. Spec. Publ., 42, 313–345, https://doi.org/10.1144/GSL.SP.1989.042.01.19, 1989.

Tang. J., Xu. W. L., Wang. F., and Ge. W.C.: Subduction history of the Paleo-Pacific slab beneath Eurasian continent: Mesozoic-Paleogene magmatic records in Northeast Asia, Sci. China. Earth. Sci., 61, 527–559, https://doi.org/CNKI:SUN:JDXG.0.2018-05-003, 2018.

Trail, D., Watson, E. B., and Tailby, N. D.: Ce and Eu anomalies in zircon as proxies for the oxidation state of magmas, Geochim. Cosmochim. Ac., 97, 70–87, https://doi.org/10.1016/j.gca.2012.08.032, 2012.

Vervoort, J.D., and Blichert-Toft, J.: Evolution of the depleted mantle: Hf isotope evidence from juvenile rocks through time, Geochim. Cosmochim. Ac., 63(3), 533–556, https://doi.org/10.1016/S0016-7037(98)00274-9, 1999.

Wan, Y.S., Song, B., Liu, D.Y., Wilde, S. A., Wu, J.S., Shi, Y.R., Yin, X.Y., and Zhou, H.Y.: 2006. SHRIMP U-Pb zircon geochronology of Palaeoproterozoic

991   metasedimentary rocks in the North China Craton: Evidence for a major Late

992   Palaeoproterozoic tectonothermal event, Precambrian. Res., 149, 271, https://doi.org/10.1016/j.precamres.2006.06.006, 2006.

993   https://doi.org/10.1016/j.precamres.2006.06.006, 2006.

994   Wang, F., Liu, F., Schertl, H.P., Xu, W., Liu, P., and Tian, Z.: Detrital zircon U-Pb

995   geochronology and Hf isotopes of the Liaohe Group, Jiao-Liao-Ji Belt:

996   Implications for the Paleoproterozoic tectonic evolution, Precambrian. Res., 340,

997   105633, 10.1016/j.precamres.2020.105633, 2020b.

998   Wang, N., Wu, C. L, Lei, M., and Chen, H.J.: Petrogenesis and tectonic implications of

999   the Early Paleozoic granites in the western segment of the North Qilian orogenic

1000   belt, China, Lithos, 312–313, 89–107, https://doi.org/10.1016/j.lithos.2018.04.023,

1001   2018.

1002   Wang, Q., Xu, J. F., Jian, P., Bao Z. W., Zhao. Z. H., Li. C. F., Xiong. X. L., and Ma,

1003   J. L.: Petrogenesis of adakitic porphyries in an extensional tectonic setting, Dexing,

1004   South China: Implications for the genesis of porphyry copper mineralization, J.

1005   Petrol., 47(1), 119–144, https://doi.org/10.1093/petrology/egi070, 2006.

1006   Wang, X. P., Oh, C. W., Peng, P., Zhai, M. G., Wang, X. H., and Lee, B. Y.:

1007   Distribution pattern of age and geochemistry of 2.18-2.14 Ga I- and A-type

1008   granites and their implication for the tectonics of the Liao-Ji belt in the North

1009   China Craton, Lithos, 364–365, 105518,

1010   https://doi.org/10.1016/j.lithos.2020.105518, 2020a.

1011   Wang, X., Griffin, W. L., Chen, J., Huang, P.Y., and Li, X.: U and Th contents and

1012   Th/U ratios of zircon in felsic and mafic magmatic rocks: Improved zircon-melt

45

distribution coefficients, Acta. Geol. Sin. Engl., 85, 164–174, https://doi.org/10.1111/j.1755-6724.2011.00387.x, 2011.

Wang, X., Griffin, W. L., O'Reilly, S. Y., and Li, W.X.: Three stages of zircon growth in magmatic rocks from the Pingtan Complex, eastern China, Acta. Geol. Sin. Engl., 81, 68–80, https://doi.org/10.3321/j.issn:1000-9515.2007.01.008, 2007.

Wang, X.L., Lv, X., Liu, Y.J., Zhao, Y.Y., Li, C., Wu, W.B., Wang, Y.P., and Li, H.Y.: LA-ICP-MS zircon U-Pb ages, geochemical characteristics of Late Triassic intrusives in Xiuyan area, eastern Liaoning and their geological significances, Ore. Geol. Rev., 65, 401–416, https://doi.org/10.16509/j.georeview.2019.02.010, 2019.

Watson, E. B., and Harrison, T. M.: Zircon saturation revisited: temperature and composition effects in a variety of crustal magma types, Earth. Planet. Sci. Lett., 64, 295–304, https://doi.org/10.1016/0012-821X(83)90211-X, 1983.

Watson, E. B., and Harrison, T. M.: Zircon thermometer reveals minimum melting conditions on earliest Earth, Science, 308, 841–844, https://doi.org/10.1126/science.1110873, 2005.

Whalen, J. B., Currie, K. L., and Chappell, B. W.: A-type granites: geochemical characteristics, discrimination and petrogenesis, Contrib. Mineral. Petr., 95, 407–419, https://doi.org/10.1007/BF00402202, 1987.

Wolf, M. B., and London, D.: Apatite dissolution into peraluminous haplogranitic melts: An experimental study of solubilities and mechanisms, Geochim. Cosmochim. Acta., 58, 4127–4145. https://doi.org/10.1016/0016-7037(94)90269-0, 1994.

Wu, F. Y., Jahn, B. M., Wilde, S. A., Lo, C. H., Yui, T. F., Lin, Q., Ge, W. C., and Sun,

D. Y: Highly fractionated I-type granites in NE China (I): geochronology and petrogenesis, Lithos, 66, 241–273, https://doi.org/10.1016/s0024-4937(02)00222-0, 2003.

Wu, F. Y., Liu, X. C., Ji, W. Q., Wang, J. M., and Yang, L.: Highly fractionated granites: Recognition and research, Sci. China. Earth. Sci., 60, 1201–1219, https://doi.org/10.1007/s11430-016-5139-1, 2017.

Wu, F. Y., Yang, J. H., and Liu, X. M.: Geochronological framework of the Mesozoic granitic magmatism in the Liaodong Peninsula, Northeast China (in Chinese with English abstract), Geol. J. China. Univ., 11, 305–317, 2005b.

Wu, F.Y., Han, R.H., Yang, J.H., Wilde, S. A., Zhai, M.G., and Park, S. C.: Initial constraints on the timing of granitic magmatism in North Korea using U-Pb zircon geochronology, Chem. Geol., 238, 232–248, https://doi.org/10.1016/j.chemgeo.2006.11.012, 2007.

Wu, F.Y., Lin, J.Q., Wilde, S. A., Zhang, X.O., and Yang, J.H.: Nature and significance of the Early Cretaceous giant igneous event in eastern China, Earth. Planet. Sci. Lett., 233, 103–119, https://doi.org/10.1016/j.epsl.2005.02.019, 2005c.

Wu, F.Y., Yang, J.H., Wilde, S. A., and Zhang, X.O.: Geochronology, petrogenesis and tectonic implications of Jurassic granites in the Liaodong Peninsula, NE China, Chem. Geol., 221, 127–156, https://doi.org/10.1016/j.chemgeo.2005.04.010, 2005a.

Wu, F.Y., Yang, Y.H., Xie, L.W., Yang, J.H., and Xu, P.: Hf isotopic compositions of the standard zircons and baddeleyites used in U-Pb geochronology, Chem. Geol.,

1057   234, 105–126, https://doi.org/10.1016/j.chemgeo.2006.05.003, 2006.

1058   Xu, J. F., Shinjo, R., Defant, M. J., Wang, Q., and Rapp, R. P.: Origin of Mesozoic

1059   adakitic intrusive rocks in the Ningzhen area of east China: partial melting of

1060   delaminated lower continental crust? Geology, 30(12), 1111–1114,

1061   https://doi.org/10.1130/0091-7613(2002)0302.0.CO;2, 2002.

1062   Xue, J. X., Liu, Z. H., Liu, J. X., Dong, X. J., Feng, F., and Lian, G. H.: Geochemistry,

1063   Geochronology, Hf isotope and Tectonic Significance of the Late Jurassic Huangdi

1064   Pluton in Xiuyan, Liaodong Penins (in Chinese with English abstract), Earth

1065   Science, 46(6), 2030–2043, https://doi.org/10.3799/dqkx.2020.008，2020.

1066   Xue, S., Ling, M. X., Liu, Y. L., Zhang, H., and Sun, W.D.: The genesis of early

1067   Carboniferous adakitic rocks at the southern margin of the Alxa Block, North

1068   China, Lithos, 278–281, 181–194, https://doi.org/10.1016/j.lithos.2017.01.012,

1069   2017.

1070   Yang, F.C., Song, Y.H., Hao, L.B., and Peng, C.: Late Jurassic SHRIMP U-Pb age and

1071   Hf isotopic characteristics of granite from the Sanjiazi Area in Liaodong and their

1072   geological significance (in Chinese with English abstract), Acta. Geol. Sin. Engl.,

1073   89, 1773–1782, 2015a.

1074   Yang, F.C., Song, Y.H., Yang, J.L., Shen, X., and Gu, Y.C.: SHRIMP U-Pb age and

1075   geochemical characteristics of granites in Wulong-Sidaogou Gold Deposit, East

1076   Liaoning (in Chinese with English abstract), Geotectonica et Metallogenia, 42,

1077   940–954, https://doi.org/10.16539/j.ddgzyckx.2018.05.010, 2018.

1078   Yang, J. H., Wu, F. Y., Xie, L. W., and Liu, X. M.: Petrogenesis and tectonic

implications of Kuangdonggou synites in the Liaodong Peninsula, east North China Craton: Constraints from in-suit zircon U-Pb ages and Hf isotopes (in Chinese with English abstract), Acta. Petrol. Sin., 23, 263–276, https://doi.org/10.1016/j.sedgeo.2006.03.028, 2007.

Yang, J.H., Wu, F.Y., Lo, C.H., Chung, S.L., Zhang, Y,B., and Wilde, S.A.: Deformation age of Jurassic granites in the Dandong area, eastern China: Ar-40/Ar-39 geochronological constraints (in Chinese with English abstract), Acta. Petrol. Sin., 20(5), 1205–1214, 2004.

Yang, M. C., Chen, B., and Yan, C.: Petrological, geochronological, geochemical and Sr-Nd-Hf isotopic constraints on the petrogenesis of the Shuangcha Paleoproterozoic megaporphyritic granite in the southern Jilin Province: Tectonic implications (in Chinese with English abstract), Acta. Petrol. Sin., 31, 1573–1588, 2015b.

Yang, M.C., Chen, B., and Yan, C.: Paleoproterozoic Gneissic Granites in the Liaoji Mobile Belt, North China Craton: Implications for Tectonic Setting. In: Zhai M., Zhao Y., Zhao T. (eds) Main Tectonic Events and Metallogeny of the North China Craton, Springer. Geology. Springer. Singapore., 155–180, https://doi.org/10.1007/978-981-10-1064-4_7, 2016.

Yu, S., Zhang, J., and Del Real, P. G.: Geochemistry and zircon U-Pb ages of adakitic rocks from the Dulan area of the North Qaidam UHP terrane, north Tibet: constraints on the timing and nature of regional tectonothermal events associated with collisional orogeny, Gondwana. Res., 21, 167–179,

https://doi.org/10.1016/j.gr.2011.07.024, 2012.

Yuan, H.L., Gao, S., Dai, M.N., Zong, C.L., Günther, D., Fontaine, G.H., Liu, X.M., and Diwu, C.R.: Simultaneous determinations of U-Pb age, Hf isotopes and trace element compositions of zircon by excimer laser-ablation quadrupole and multiple-collector ICP-MS, Chem. Geol., 247, 100–118, https://doi.org/10.1016/j.chemgeo.2007.10.003, 2008.

Yuan, L. L., Zhang, X. H., Xue, F. H., Han, C. M., Chen, H. H., and Zhai, M. G.: Two episodes of Paleoproterozoic mafic intrusions from Liaoning province, North China Craton: Petrogenesis and tectonic implications, Precambrian. Res., 264, 119–139, https://doi.org/10.1016/j.precamres.2015.04.017, 2015.

Zeng, R.Y., Lai, J.Q., Mao, X.C., Li, B., Ju, P.J., and Tao, S.L.: Geochemistry, zircon U-Pb dating and Hf isotopies composition of Paleozoic granitoids in Jinchuan, NW China: Constraints on their petrogenesis, source characteristics and tectonic implication, J. Asian. Earth. Sci., 121, 20–33, https://doi.org/10.1016/j.jseaes.2016.02.009, 2016.

Zeng, R.Y., Lai, J.Q., Mao, X.C., Li, B., Zhang, J.D., Bayless, R., and Yang, L.Z.: Paleoproterozoic Multiple Tectonothermal Events in the Longshoushan Area, Western North China Craton and Their Geological Implication: Evidence from Geochemistry, Zircon U-Pb Geochronology and Hf Isotopes, Minerals. Basel., 8, https://doi.org/10.3390/MIN8090361, 2018.

Zhai, M.G., Meng, Q.R., Liu, J.M., Hou, Q.L., Hu, S.B., Li, Z., Zhang, H.F., Liu, W., Shao, J.A., and Zhu, R.X.: Geological features of Mesozoic tectonic regime

1123 inversion in eastern North China and implication for geodynamics, Earth. Science.

1124 Frontiers., 11, 285–298, https://doi.org/10.3321/j.issn:1005-2321.2004.03.027,

1125 2004.

1126 Zhan, Q. Y., Zhu, D. C., Wang, Q., Weinberg, R. F., Xie, J. C., Li, S. M., Zhang, L.L.,

1127 and Zhao, Z. D.: Source and pressure effects in the genesis of the Late Triassic

1128 high Sr/Y granites from the Songpan-Ganzi Fold Belt, eastern Tibetan Plateau,

1129 Lithos, 368–369, https://doi.org/10.1016/j.lithos.2020.105584, 2020.

1130 Zhang, B., Guo, F., Zhang, X. B., Wu, Y.M., Wang, G.Q., and Zhao, L.: Early

1131 Cretaceous subduction of Paleo-Pacific Ocean in the coastal region of SE China:

1132 Petrological and geochemical constraints from the mafic intrusions, Lithos, 334–

1133 335, 8–24, https://doi.org/10.1016/j.lithos.2019.03.010, 2019.

1134 Zhang, Q., Qian, Q., Wang, E.Q., Wang, Y., Zhao, T.P., Hao, J., and Guo, G.J.: An

1135 East China plateau in mid-late Yanshanian period: implication from adakites,

1136 Chinese (in Chinese with English abstract). Chinese Journal of Geology, 36 (2),

1137 248–255, 2001.

1138 Zhang, Q., Wang, Y., Liu, H., and Wang, Y.: On the space-time distribution and

1139 geodynamic environments of adakites in China annex: controversies over differing

1140 opinions for adakites in China (in Chinese with English abstract), Earth Science

1141 Frontiers, https://doi.org/10.1016/S0955-2219(02)00073-0, 2003.

1142 Zhang, S., Zhu, G., Xiao, S.Y., Su, N., Liu, C., Wu, X.D., Yin, H., Li, Y.J., and Lu,

1143 Y.C.: Temporal variations in the dynamic evolution of an overriding plate:

1144 Evidence from the Wulong area in the eastern North China Craton, China, Geol.

1145   Soc. Am. Bull., 132(9–10), 2023–2042, https://doi.org/10.1130/B35465.1, 2020.

1146   Zhao, K.D., Jiang, S.Y., Ling, H.F., and Palmer, M. R.: Reliability of LA-ICP-MS U-

1147   Pb dating of zircons with high U concentrations: A case study from the U-bearing

1148   Douzhashan Granite in South China, Chem. Geol., 389, 110–121,

1149   https://doi.org/10.1016/j.chemgeo.2014.09.018, 2014.

1150   Zhao, K.D., Jiang, S.Y., Ling, H.F., and Palmer, M. R.: Reliability of LA-ICP-MS U-

1151   Pb dating of zircons with high U concentrations: A case study from the U-bearing

1152   Douzhashan Granite in South China, Chem. Geol., 389, 110–121,

1153   https://doi.org/10.1016/j.chemgeo.2014.09.018, 2014.

1154   Zheng, J.P., and Dai, H.K.: Subduction and retreating of the western Pacific plate

1155   resulted in lithospheric mantle replacement and coupled basinmountain respond in

1156   the North China Craton, Sci. China. Earth. Sci., 61, 406–424,

1157   https://doi.org/10.1007/s11430-017-9166-8, 2018.

1158   Zheng, Y.F., Xu, Z.F., Zhao, Z.F., and Dai, L.Q.: Mesozoic mafic magmatism in North

1159   China: Implications for thinning and destruction of cratonic lithosphere, Sci. China.

1160   Earth Sci., 61, 353–385, https://doi.org/10.1007/s11430-017-9160-3, 2018.

1161   Zhu, R. X., and Xu, Y. G.: The subduction of the west Pacific plate and the destruction

1162   of the North China Craton, Sci. China. Earth Sci., 62, https://doi.org/1340-1350,

1163   10.1007/s11430-018-9356-y, 2019.

1164   Zhu, R.X., and Xu, Y.G.: The subduction of the west Pacific plate and the destruction

1165   of the North China Craton, Sci. China. Earth. Sci., 62, 1340–1350,

1166   https://doi.org/10.1007/s11430-018-9356-y, 2019.

1167 **Table captions**

1168 Table S1. Major element (wt. %) and trace element (ppm) compositions of the

1169 Zhoujiapuzi granite

1170 Table S2. Raman microprobe data

1171 Table S3. The zircon major element (wt. %) and trace element (ppm) from the

1172 Zhoujiapuzi granite

1173 Table S4. Zircon La-ICP-MS U-Pb isotopic data and ages of the Zhoujiapuzi granite

1174 Table S5. Zircon Hf isotopic data of the Zhoujiapuzi granite
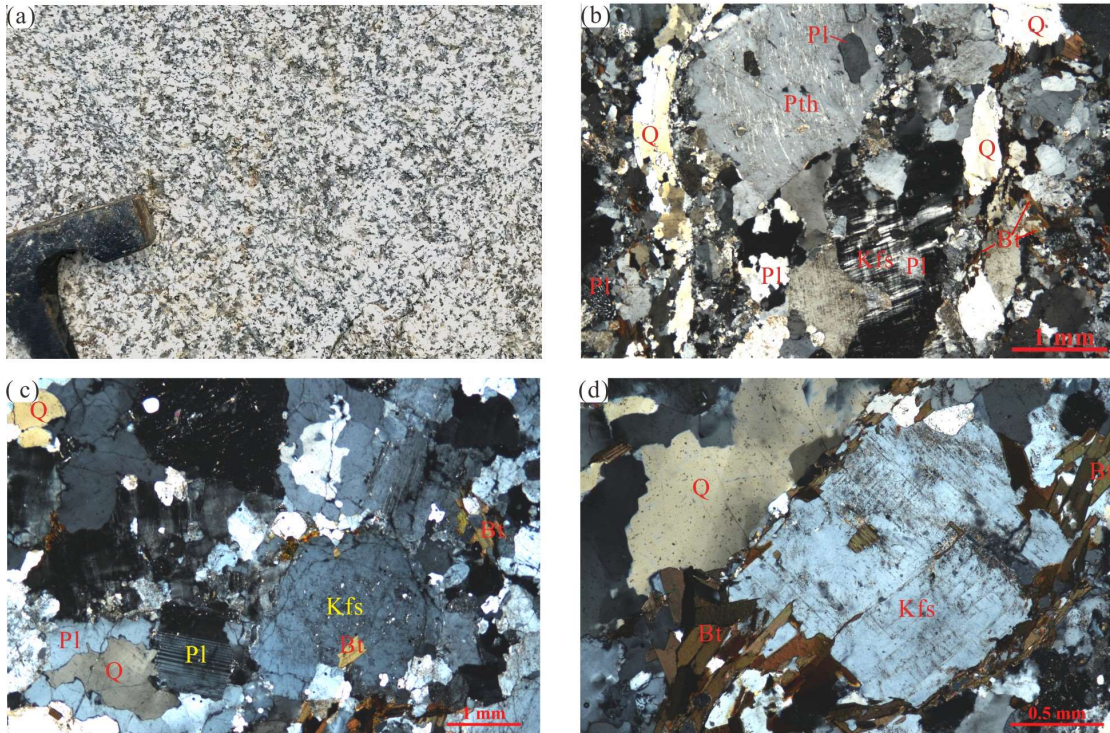
1175

1176 **Figure captions**
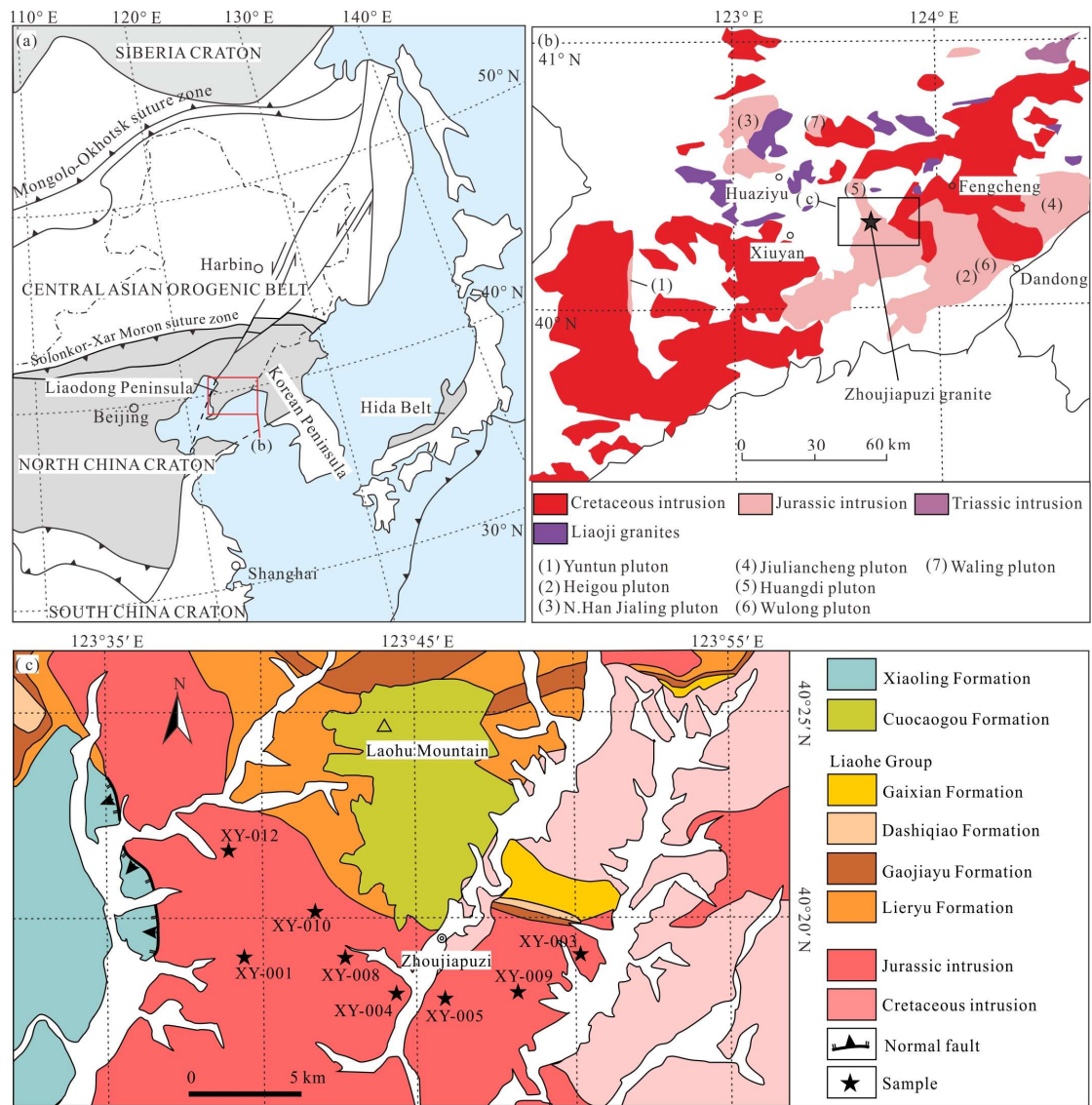
Figure 1. (a) Simplified geological map of Northeast China (Modified from Li et al., 2016); (b) distribution of Mesozoic intrusions in the Liaodong Peninsula (Modified from Wu et al., 2005a); (c) geological map of the Zhoujiapuzi granite.

1182

1183 Figure 2. Outcrop photograph (a) and corresponding micrographs (b, c, d-

1184 perpendicular polarized light). Q quartz; Kfs feldspar; Pl plagioclase; Pth perthite; Bt

1185 biotite

1186

○ Zhoujiapuzi granite (this study)
+ Other middle-late Jurassic granitoids (165−156 Ma) in Liaodong Peninsula
  (Wu et al., 2005a; Yang et al., 2015b, 2018; Xue et al., 2020)
◇ Muniuhe granitic pluton (Yang et al., 2016; Wang et al., 2020a)
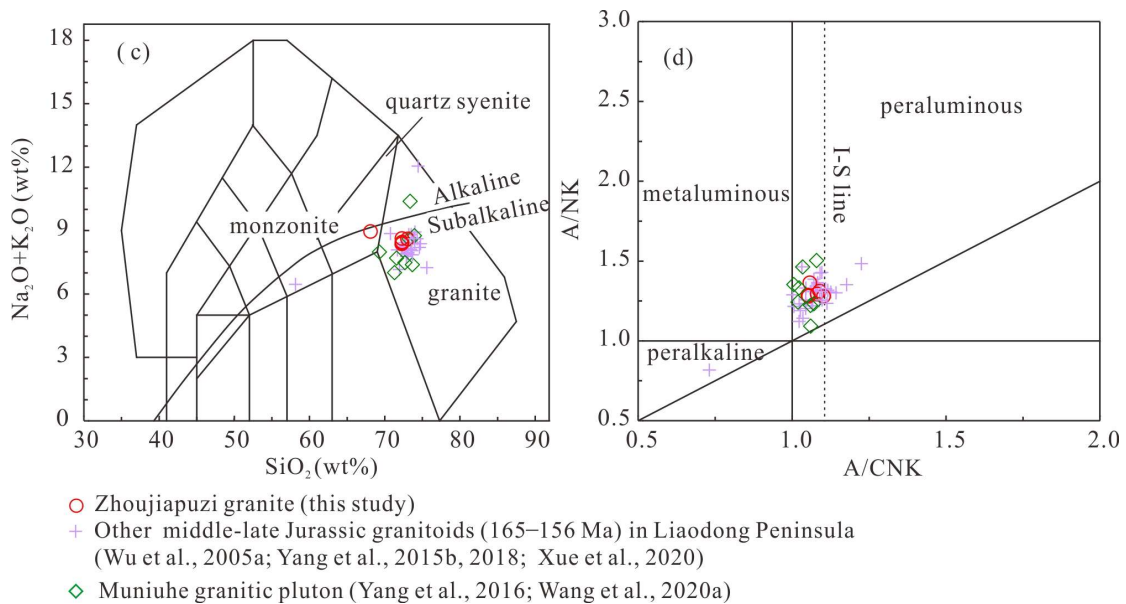
1187

1188 Figure 3. Geochemical classification diagrams for the Zhoujiapuzi granite. (a) TAS

1189 diagram (after Frost et al.，2001); (b)A/CNK-A/NK diagram (after Maniar and

55

Piccoli, 1989)
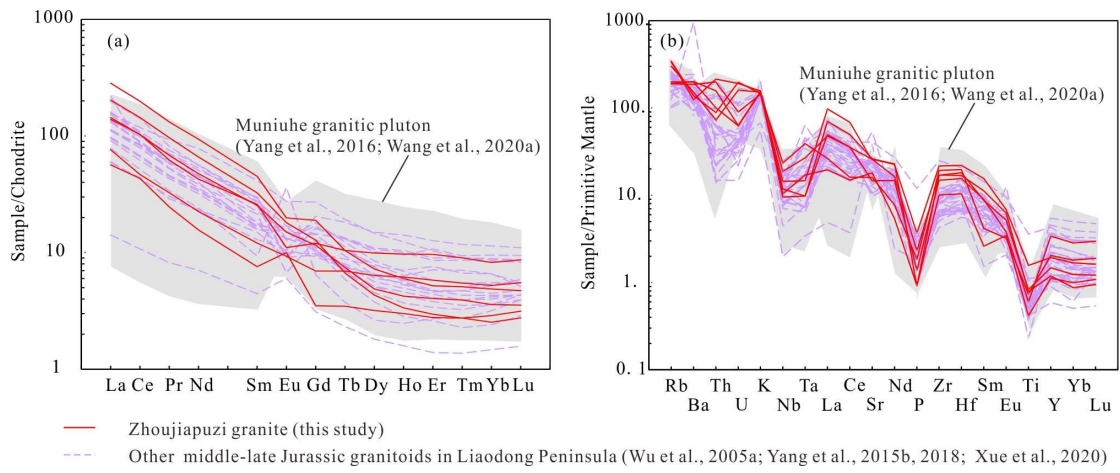
Figure 4. Chondrite-normalized REE patterns and primitive mantle-normalized trace

element patterns of the Zhoujiapuzi granite (chondrite and primitive mantle values are

from Sun and McDonough, 1989).
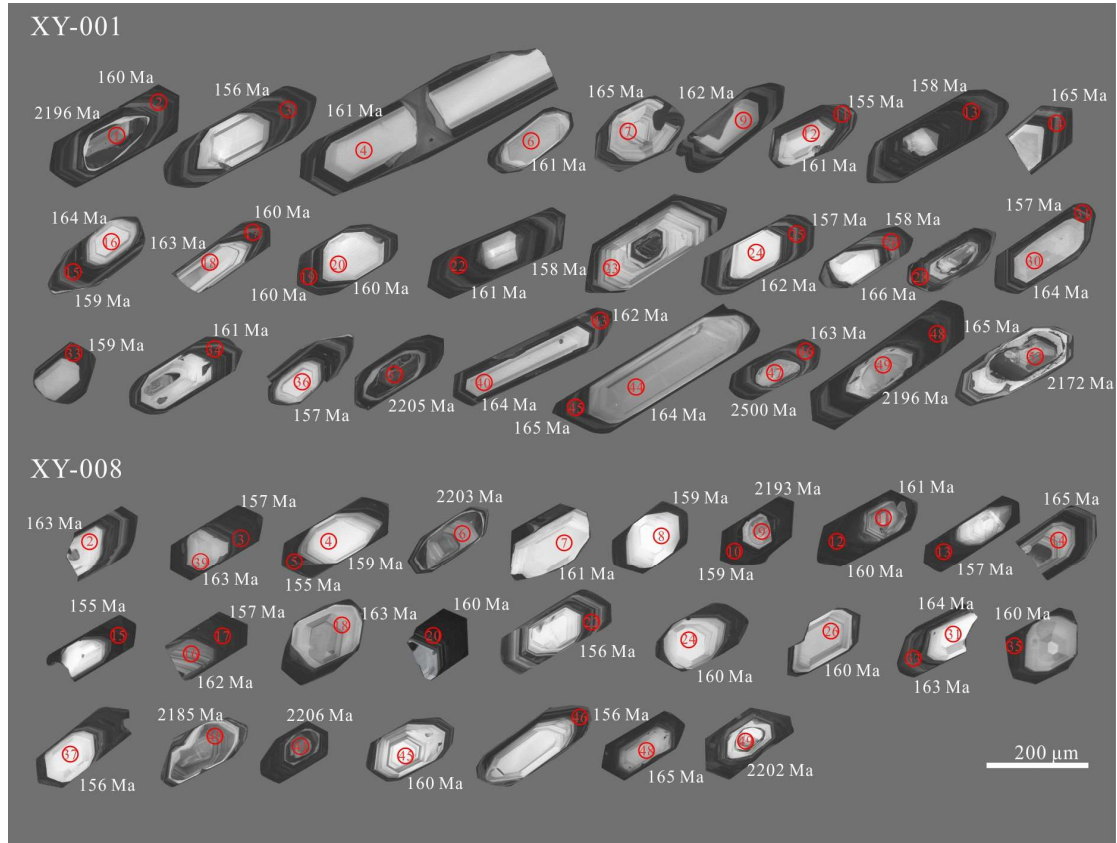
Figure 5. CL images of zircons. Circles denote U-Pb analysis spot. Numbers in the

1199   circles are the spot numbers. Numbers near the analytical spots are the U–Pb ages

1200   (Ma).

1201
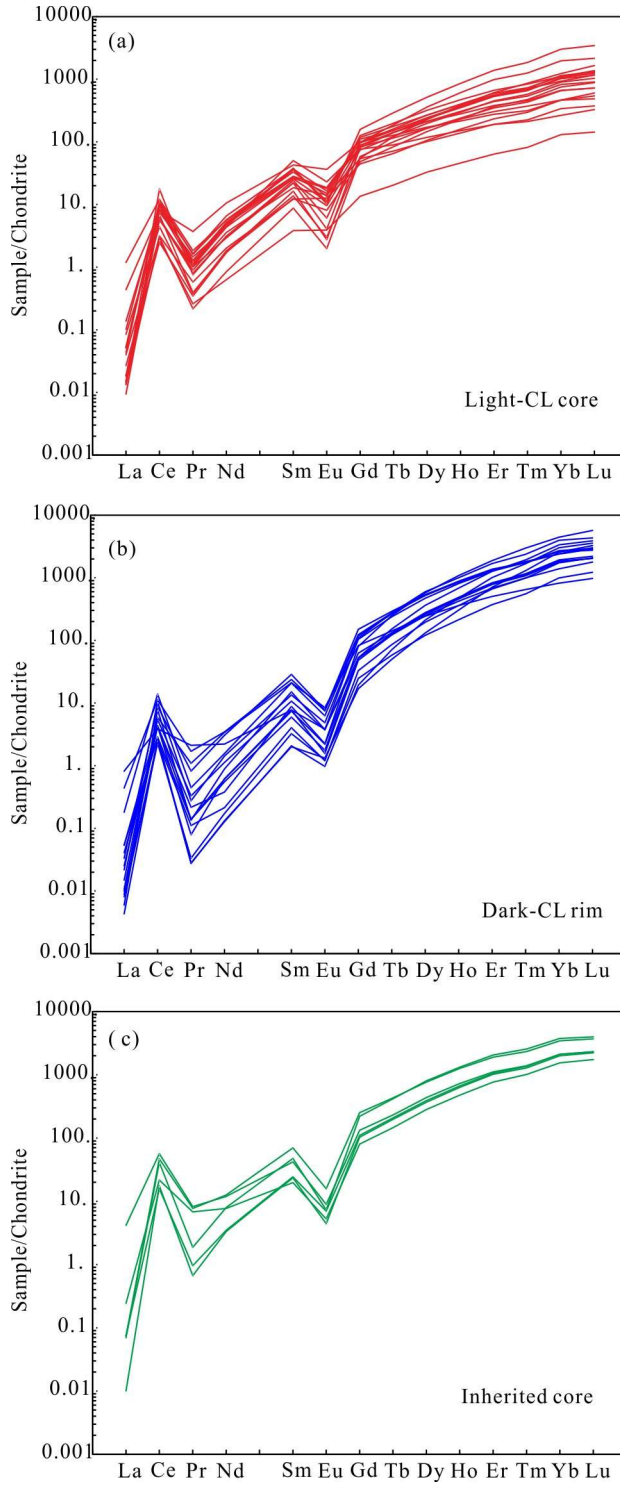
1202

1203   Figure 6. Chondrite-normalized REE patterns of zircon (chondrite values are from

1204   Sun and McDonough, 1989).
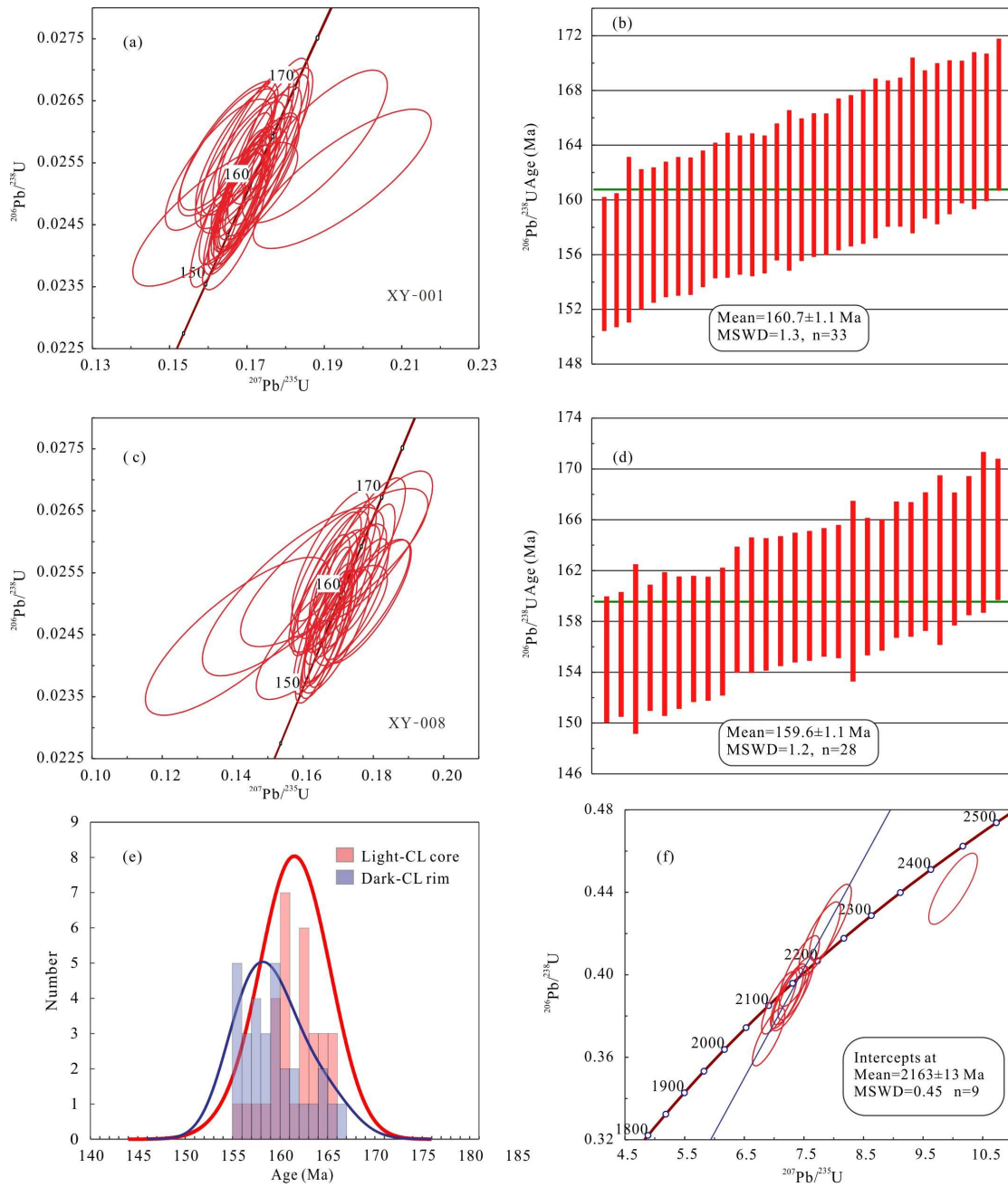
Figure 7. Concordia diagrams for zircon LA-ICP-MS U-Pb analyses.

1208

58
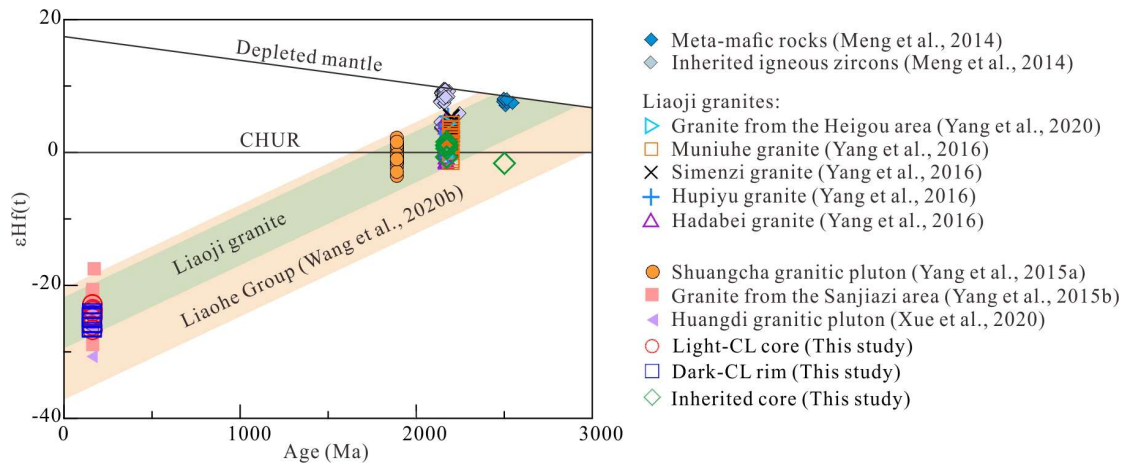
1209
1210 Figure 8. Zircon εHf(t)-age (Ma) diagram for samples in this study and published data

1211 for the region.

1212
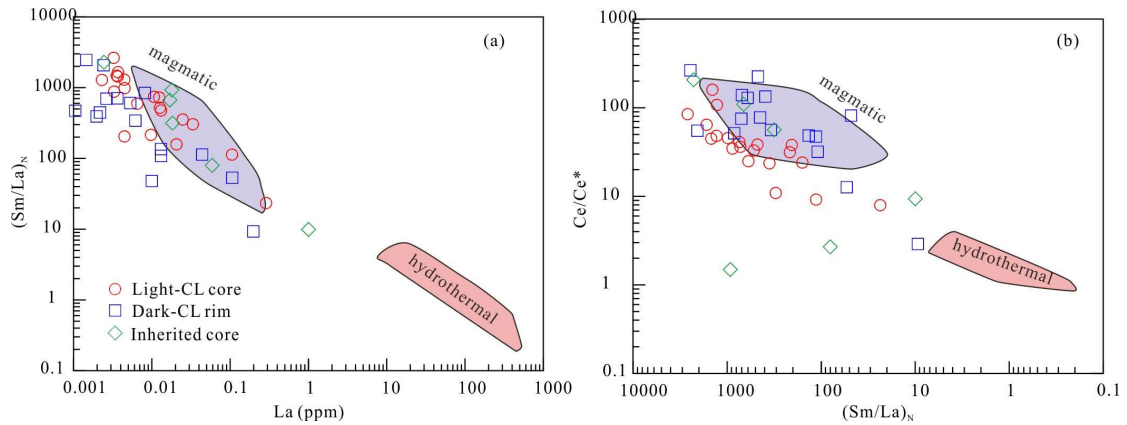
1213
1214 Fig. 9. Discrimination plots for magmatic and hydrothermal zircon (Hoskin, 2005).

1215
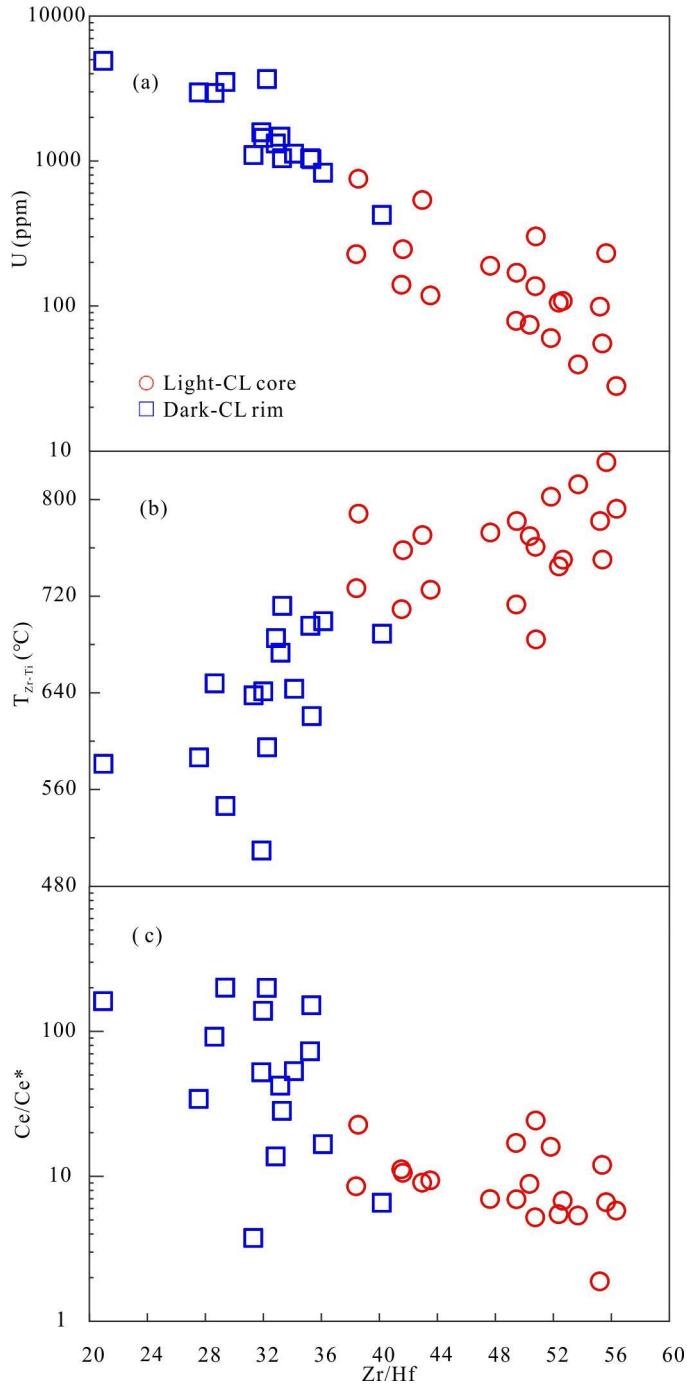
Figure 10. Covariation diagrams for zircon from the Zhoujiapuzi granite. (a) U vs. Zr/Hf; (b) T_{Zr-Ti} vs. Zr/Hf; (c) Ce/Ce* vs. Zr/Hf.
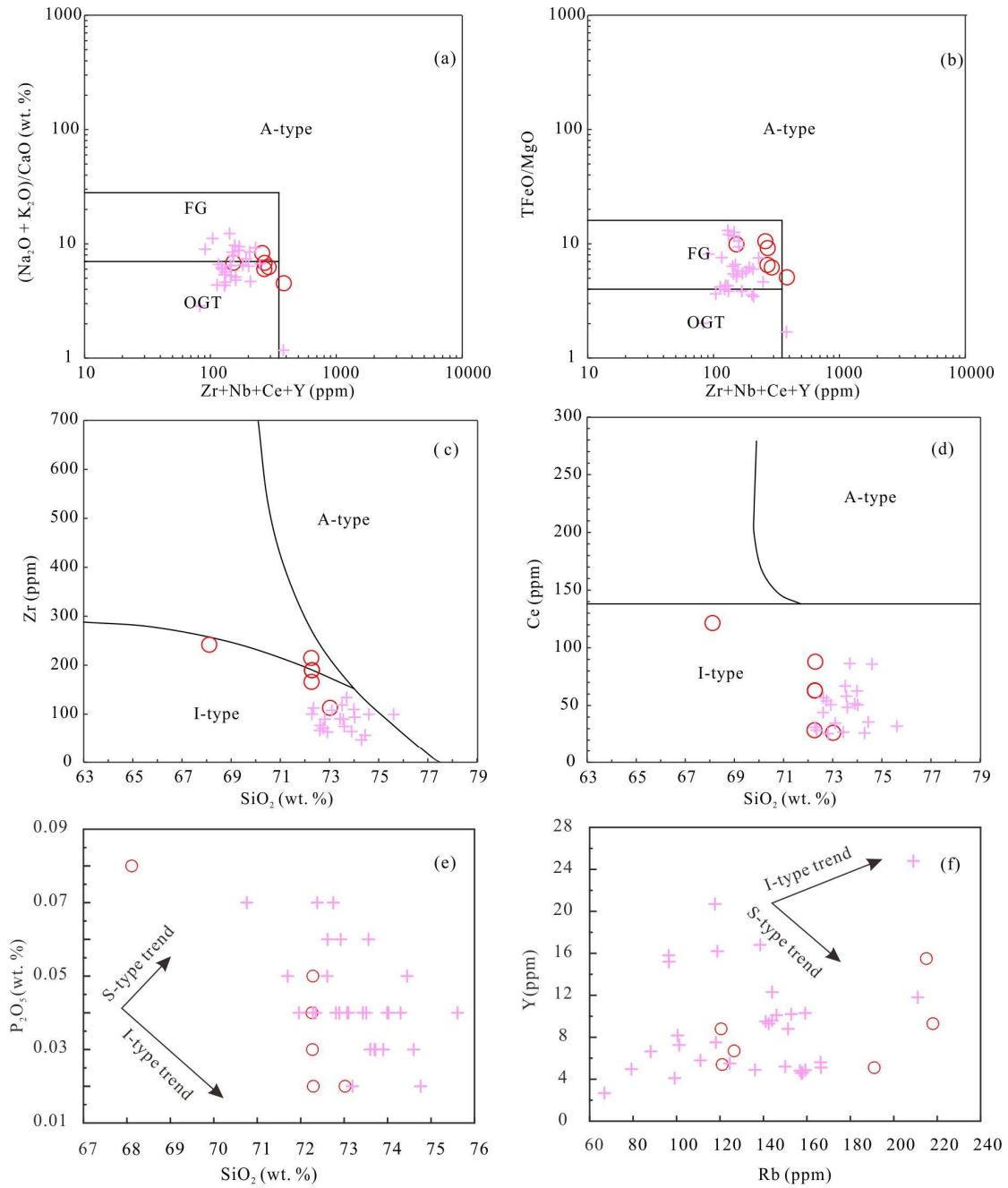
○ Zhoujiapuzi granite (this study)
+ Other middle-late Jurassic granitoids in Liaodong Peninsula (Wu et al., 2005a; Yang et al., 2015b, 2018; Xue et al., 2020)

Figure 11. Chemical variation diagrams for the Zhoujiapuzi granite. (a and b)

Zr+Nb+Ce+Y vs. $(Na_2O + K_2O)/CaO$ and $TFeO/MgO$ (after Whalen et al., 1987); (c

and d) SiO_2 vs. Zr and Ce (after Collins et al., 1982); (e) SiO_2 vs. P_2O_5 diagram; (f)
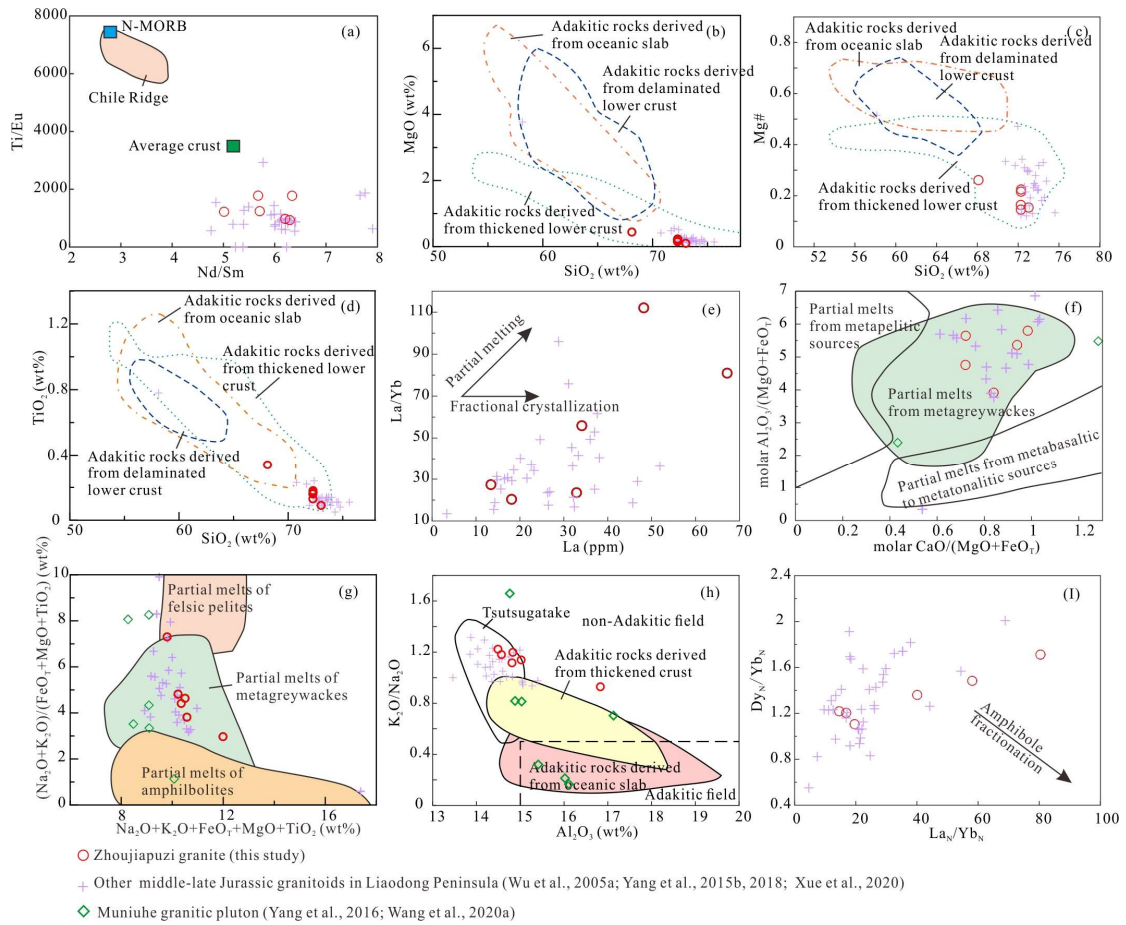
Rb vs. Y diagram
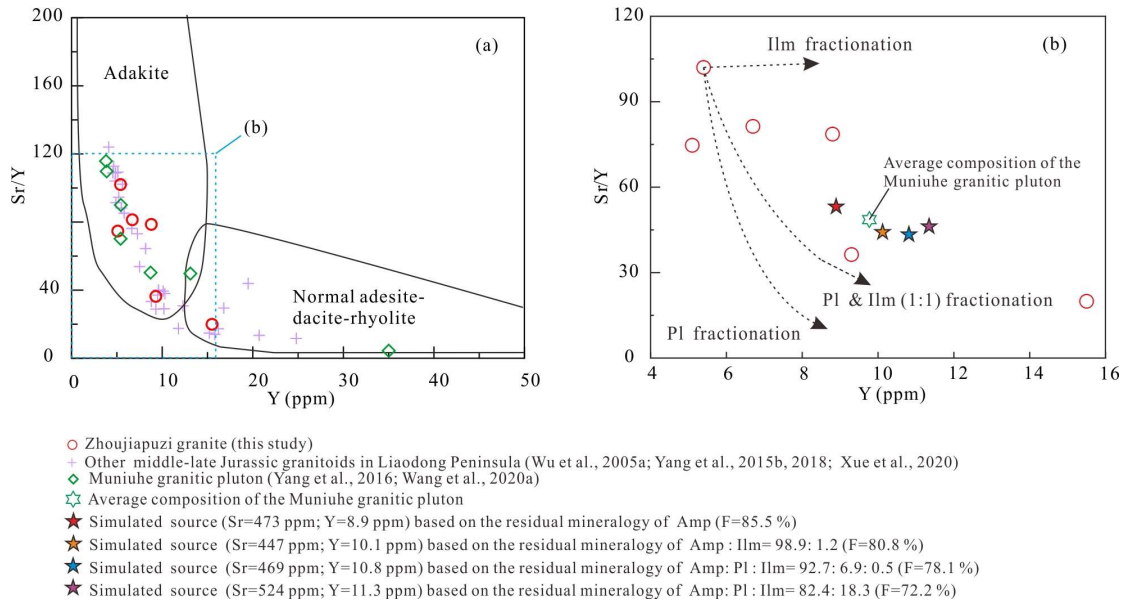
Figure 12. Adakite discrimination diagrams for the Zhoujiapuzi granite (after Defant and Drummond, 1990).

Figure 13. Source characteristics (a-d and f-h) and crystal fractionation (e and i)

discrimination diagrams for the Zhoujiapuzi granite. Plots of (a) Nd/Sm vs. Ti/Eu (Yu et al., 2012); (b-d) SiO_2 vs. MgO, Mg# and TiO_2 (after Wang et al., 2006); (e) La vs. La/Yb (Gao et al., 2007); (f) molar Al_2O_3/($MgO+FeO_T$) vs. molar CaO/($MgO+FeO_T$) (after Altherr et al., 2000); (g) (Na_2O+K_2O)/($FeO_T+MgO+TiO_2$) vs. $Na_2O+K_2O+FeO_T+MgO+TiO_2$ (after Patiño Douce, 1999); (h) K_2O/Na_2O vs. Al_2O_3 diagrams (after Kamei et al., 2009); (i) La_N/Yb_N vs. Dy_N/Yb_N.
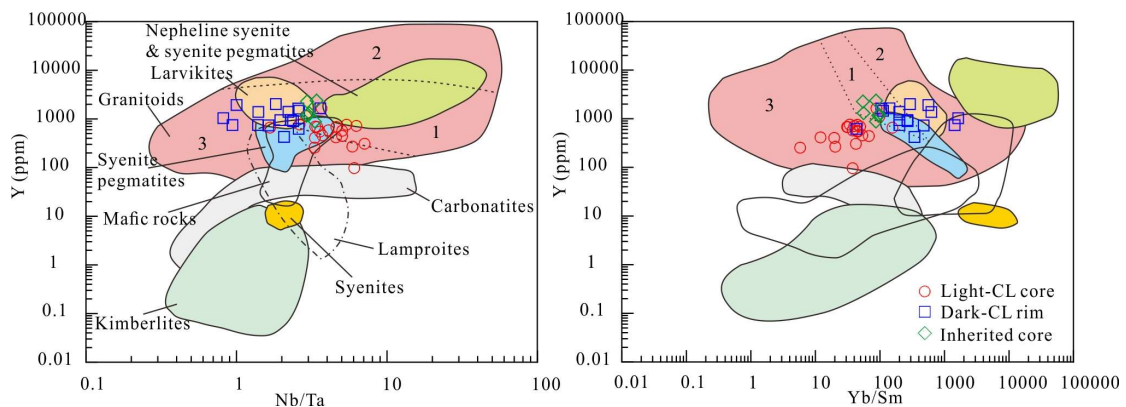
Figure 14. The fields of zircon compositions used as discriminants for different rock types (after Belousova et al., 2002). 'Granitoids' include: 1 aplites and leucogranites; 2 granites; 3 granodiorites and tonalities